RESEARCH ARTICLE

Compositional variations and magma mixing in the 1991 eruptions of Hudson volcano, Chile

**David J Kratzmann · Steven Carey · Roberto Scasso ·
Jose-Antonio Naranjo**

Abstract The August 1991 eruptions of Hudson volcano
produced ~2.7 km^3 (dense rock equivalent, DRE) of basaltic
to trachyandesitic pyroclastic deposits, making it one of the
largest historical eruptions in South America. Phase 1 of the
eruption (P1, April 8) involved both lava flows and a
phreatomagmatic eruption from a fissure located in the NW
corner of the caldera. The paroxysmal phase (P2) began
several days later (April 12) with a Plinian-style eruption
from a different vent 4 km to the south-southeast. Tephra
from the 1991 eruption ranges in composition from basalt
(phase 1) to trachyandesite (phase 2), with a distinct gap
between the two erupted phases from 54–60 wt% SiO_2. A
trend of decreasing SiO_2 is evident from the earliest part of
the phase 2 eruption (unit A, 63–65 wt% SiO_2) to the end

(unit D, 60–63 wt% SiO_2). Melt inclusion data and textures
suggest that mixing occurred in magmas from both eruptive
phases. The basaltic and trachyandesitic magmas can be
genetically related through both magma mixing and fractional
crystallization processes. A combination of observed phase
assemblages, inferred water content, crystallinity, and geo-
thermometry estimates suggest pre-eruptive storage of the
phase 2 trachyandesite at pressures between ~50–100 mega-
pascal (MPa) at 972±26°C under water-saturated conditions
(log fO_2 –10.33 (±0.2)). It is proposed that rising P1 basaltic
magma intersected the lower part of the P2 magma storage
region between 2 and 3 km depth. Subsequent mixing
between the two magmas preferentially hybridized the lower
part of the chamber. Basaltic magma continued advancing
towards the surface as a dyke to eventually be erupted in the
northwestern part of the Hudson caldera. The presence of
tachylite in the P1 products suggests that some of the magma
was stalled close to the surface (<0.5 km) prior to eruption.
Seismicity related to magma movement and the P1 eruption,
combined with chamber overpressure associated with basalt
injection, may have created a pathway to the surface for the
trachyandesite magma and subsequent P2 eruption at a
different vent 4 km to the south-southeast.

D. J. Kratzmann · S. Carey
GSO/Univ. of Rhode Island, S. Ferry Rd.,
Narragansett, RI 02882, USA

S. Carey
e-mail: scarey@gso.uri.edu

R. Scasso
Dpto. de Cs. Geologicas, FCEN,
Univ. de Buenos Aires Cuidad Univ., Pab 2, 1 Piso,
1428 Buenos Aires, Argentina

J.-A. Naranjo
Serv. Nacional Geol. y Mineria, Casilla,
Santiago 10465, Chile

D. J. Kratzmann (✉) · S. Carey
Graduate School of Oceanography, South Ferry Rd.,
Narragansett, RI 02882, USA
e-mail: davidk@gso.uri.edu

Introduction

The 1991 eruption of Hudson volcano in Chile produced
4.3 km^3 bulk volume (2.7 km^3 dense rock equivalent, DRE)
of tephra fall deposits with a wide range in composition
(Naranjo et al. 1993; Scasso et al. 1994) and was one of the

largest explosive eruptions of the 20th century. Notable features of the 1991 eruption include an abrupt transition from basalt/basaltic-andesite in the first phase of the eruption to trachyandesite during the second phase, and the separation of the two source vents by a distance of ~4 km (Naranjo et al. 1993). Linear major element trends within the climactic phase products and the occurrence of banded pumice clasts (Bitschene and Fernández 1995) suggest that magma mingling and mixing played an important role during the eruption.

Compositional diversity in erupted products and disequilibrium textures in phenocrysts have been attributed to magma mixing at numerous arc-related volcanoes (e.g., Eichelberger 1975; Huppert et al. 1982; Tepley et al. 2000; Martel et al. 2006). The triggering of explosive eruptions by magma injection and subsequent mixing has also been proposed at several volcanic centers (e.g., Askja (Sparks et al. 1977); Pinatubo (Pallister et al. 1992); Soufrière Hills (Murphy et al. 1998); Karymsky (Eichelberger and Izbekov 2000)) and has previously been suggested as the mechanism responsible for the 1991 eruption of Hudson volcano (e.g., Naranjo et al. 1993). The 1991 eruption thus provides an excellent opportunity for an integrated petrological and volcanological assessment of the magma evolution and eruptive mechanisms at an important Andean arc volcano. Here we investigate the compositional diversity of the 1991 products and evaluate the genetic relationship between the two eruptive phases. In addition, we attempt to define the nature of the magmatic system beneath Hudson prior to the 1991 activity based on pressure, temperature, and volatile content estimates. A model is proposed to explain the temporal and spatial relationships of the eruption of basalt at the northwestern corner of the Hudson caldera followed by the paroxysmal eruption of trachyandesite at a different vent 4 km to the south-southeast.

Geological setting and background

Hudson volcano is the southernmost volcano of the Chilean Southern Volcanic Zone (SVZ; 33–46°S, Fig. 1). Located approximately 280 km from the Nazca-Antarctica-South American triple junction (Naranjo and Stern 1998), it is a result of the subduction of the Nazca plate beneath the South American plate. Hudson occurs just north of the

Fig. 1 **a** Tectonic map of southern South America. *Triangles* represent single currently active volcanic centers. Modified from Orihashi et al. (2004). **b** Schematic map of the caldera at the summit of Hudson and the 1991 craters and P1 fissure system. Modified from Naranjo et al. (1993). **c** Tephra fall distributions for the 1991 eruptions. The 1-cm isopach (*dashed black line*) and main dispersal axis (*arrows*) for the phase 1 and phase 2 deposits have been included to highlight the effect of local winds on tephra deposition. Sampling site 28 (L28) is situated close to the main dispersal axis of fall deposits from the P2 eruption, approximately 30 km SE of Hudson
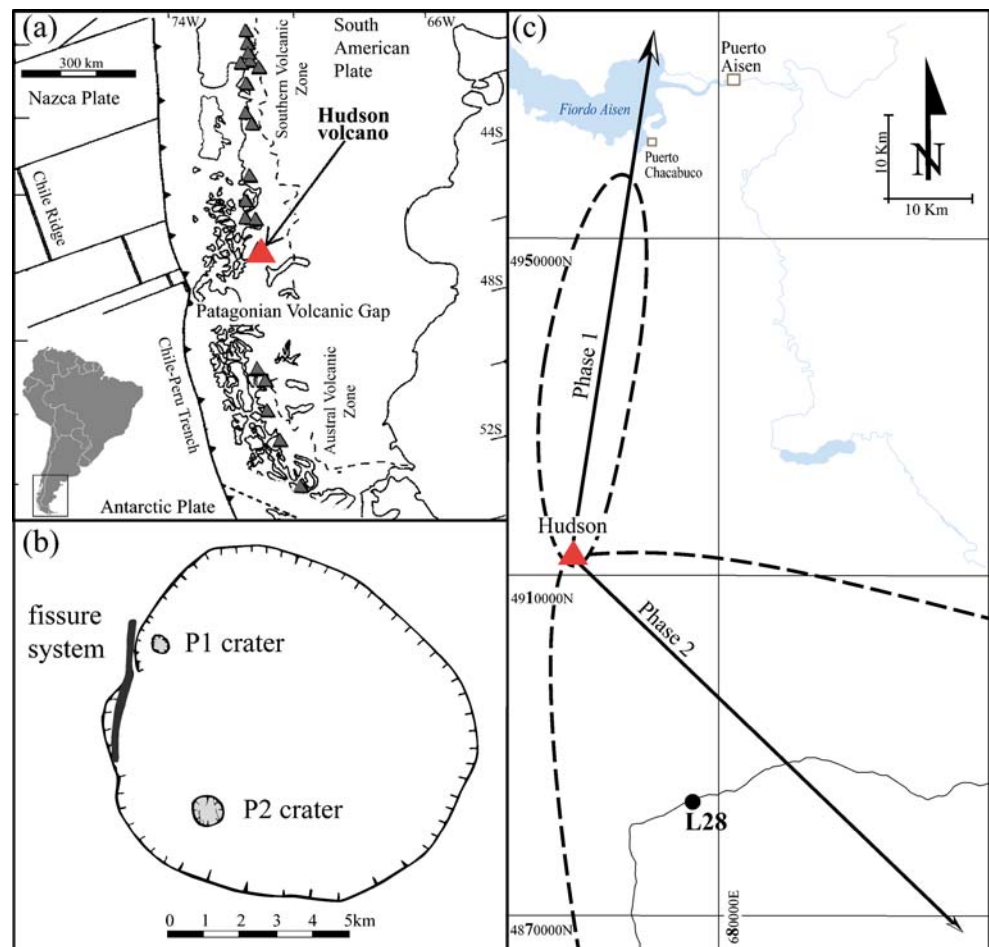
~300-km-long Patagonian Volcanic Gap (46–49°S), which is related to the subduction of the Chile Rise over the last 8 million years (Stern et al. 1984; Forsythe and Nelson 1985; Stern 2004). To the south, subduction-related volcanism resumes again in the Austral Volcanic Zone (49–55°S) (Fig. 1) (Stern 2004). K-Ar dating indicates that Hudson has been active for at least the last 1 million years (Orihashi et al. 2004). There have been at least 12 Holocene to Recent explosive eruptions (Naranjo and Stern 1998), the most significant of which were the 6,700 years before present (yrs BP), the 3,600 yrs BP, and 1991 eruptions. The 6,700 yrs BP eruption may have been the event responsible for the formation of the present caldera (Stern 1991), although Gutiérrez et al. (2005) and Orihashi et al. (2004) both suggested incremental formation over an extended period. The 10-km-diameter, almost circular caldera is filled with glacial ice, which drains into the Huemules glacier to the north (Naranjo and Stern 1998). A widespread Holocene tephra layer covers large areas of southern Chile and Argentina and has been geochemically correlated to the 6,700 yrs BP eruption (Stern 1991).

In general, Hudson magmas are medium- to high-K calc-alkaline with elevated incompatible elements (i.e., large-ion lithophile elements, LILE; rare-earth elements, REE; and high-field-strength elements, HFSE). On a total alkali versus silica plot (not shown), Hudson samples overlie the curve of Irvine and Baragaar (1971) dividing the alkaline and subalkaline fields. We have opted to follow the naming convention of previous authors (e.g., Bitschene and Fernández 1995; Naranjo and Stern 1998; Gutiérrez et al. 2005) and designate the Hudson trachyandesite as calc-alkaline. $^{87}Sr/^{86}Sr$ ratios are relatively uniform ~0.7044, although slightly higher than observed in samples from other volcanoes of the southern SVZ (Naranjo and Stern 1998). Gutiérrez et al. (2005) suggested that Hudson basaltic magmas are not primitive but are products of melting and partial assimilation processes occurring during ascent. Petrographic and textural evidence are cited as indicators for a mixed magma origin for the intermediate compositions, and fractional crystallization can explain the compositional range of Hudson products (Gutiérrez et al. 2005).

Hudson eruption

The 1991 eruption began on August 8th (18:20 hours) (P1) with both a phreatomagmatic event and lava flows through a 400-m-crater (in the surface of the glacier) and a 4-km-long, NNE-SSW trending fissure (respectively) in the northwestern corner of the caldera (Naranjo et al. 1993). The eruption column height reached 12 km and approximately 0.2 km³ (bulk volume) of tephra was deposited northeast of the vent by prevailing winds (Naranjo et al. 1993; Scasso et al. 1994) (Fig. 1). The lava flow covered

approximately 6–7 km² of the glacier. Between 21:00 to 22:00 hours jökulhaups from the Huemules glacier descended the Huemules valley for the next 10 to 12 hours (Bitschene and Fernández 1995). The paroxysmal phase of the eruption (P2) began on August 12th (12:00 hours) with a Plinian-style eruption from an 800-m-wide crater (in the ice surface) approximately 4 km to the south-southeast of the first crater. The column height reached >10 km during this phase of the eruption and stabilized at ~16 km on August 13th. The ash plume detached from the vent at 12:00 hours on August 14th (Naranjo et al. 1993; Scasso et al. 1994). The eruption recommenced at approximately 20:00 on August 14th and ceased on August 15th. Tephra from this phase was directed southeast in an elongate plume (Fig. 1), and the tephra fall deposit extended to the Malvinas Islands ~1,500 km to the south in a narrow band almost 370 km wide that covered ~100,000 km² of southern Patagonia (Scasso et al. 1994). Seismicity related to the eruption suggested that the hypocenters lay between 2 to 20 km depth (Araujo 1993; Naranjo et al. 1993), and the epicenters defined a south-southeast trend similar to that of the Linique-Ofqui fault system (Bitschene and Fernández 1995).

Samples and analytical techniques

Tephra fall deposits from the Holocene eruptions were sampled at 55 sites along the Chilean-Argentinean border over 2 weeks in January 2005 (supplementary Table S1). The stratigraphy from the paroxysmal phase of the 1991 eruption is quite complex, and many well-defined fall units are traceable up to 50 km from source (Fig. 2a). In this area, the P2 stratigraphy includes four coarse-grained fall units (A–D) (Fig. 2b). Subsequent petrographic and geochemical analyses were conducted on, but not limited to, pumice samples selected from these tephra layers. Pumice samples were cleaned in de-ionized (DI) water, sonicated for 10 min to remove any foreign particles, rinsed in DI water again, and then dried overnight at 100°C.

Whole-rock analyses of multiple pumice clasts were conducted using x-ray fluorescence analysis (XRF) with a Bruker S4 Pioneer wave-length dispersive X-ray fluorescence spectrometer at the Department of Geosciences, University of Rhode Island (URI). Precision for most elements was better than 0.2 wt% and accuracy better than 1 wt% of the measured values. Major element compositions of high-silica glasses were obtained using a Cameca MBX electron microprobe equipped with sodium migration software. Low-silica glasses and mineral phases were analyzed using a Cameca SX-100 electron microprobe. A 15-kV accelerating voltage, a 9.6-nA beam current (MBX), and 15 kV and 15 nA (SX-100) were used, both with a ~10-μm, focused beam diameter. All microprobe analyses were
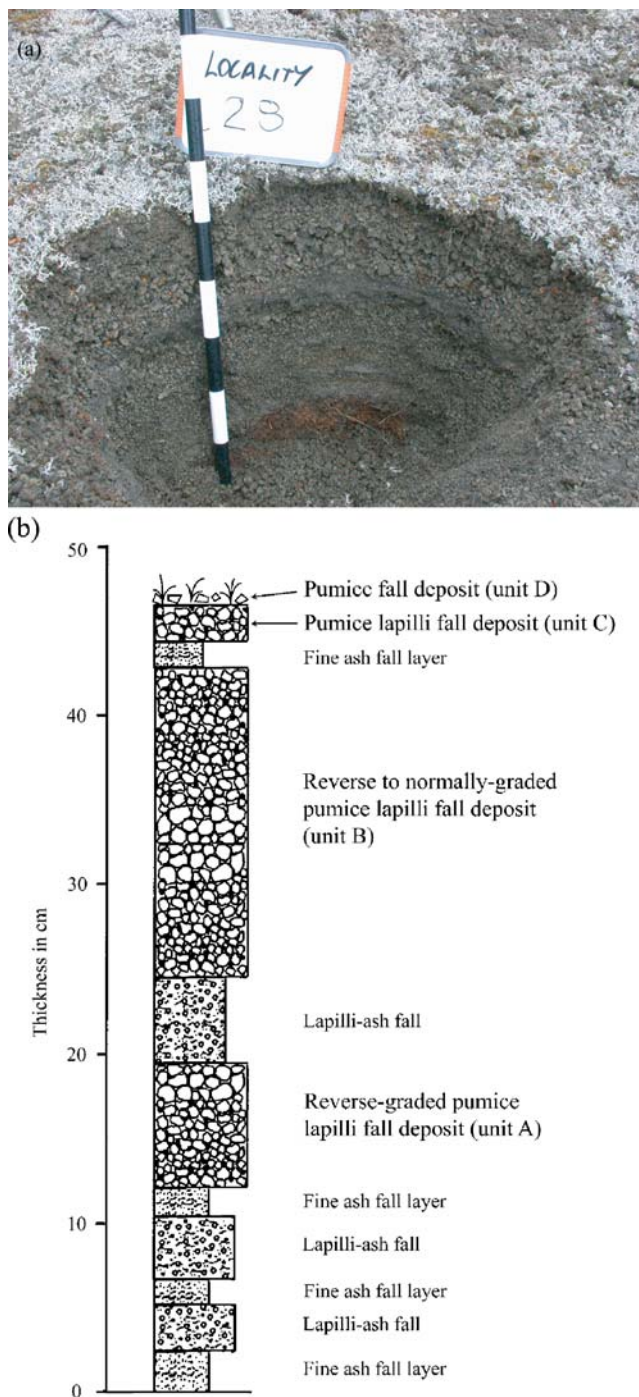
Fig. 2 a The 1991 (P2) fall deposit at sample location L28 (Fig. 1). Intervals on the scale bar in the photo are 10 cm. **b** Schematic representation of the P2 stratigraphy at sample location L28 showing the main coarse-grained fall units (A–D)

conducted at the Geological Sciences Department at Brown University using the methods described by Devine et al. (1995). Precision and accuracy were monitored by repeat analysis of well-characterized standards (e.g., KN-18) and

were better than 0.6 wt% for most elements. Water contents (transmission data) were measured on a Thermo Nicolet Nexus 670 Fourier Transform Infra Red (FTIR) spectrometer attached to a Thermo Nicolet Continuum IR microscope at the Department of Earth and Planetary Sciences, American Museum of Natural History, New York City. Modifications to the methods of Mandeville et al. (2002) include 400 scans for each IR spectrum (1,024 previously) and an increase in the range of measurements into the near-IR (7,500 cm^{-1} compared to 6,500 cm^{-1}). Trace element data were collected using the New Wave 213 nm Nd-YAG laser, attached to a Thermo X-Series II ICP-MS at the Graduate School of Oceanography (URI) following the methods of Kelley et al. (2003). Ti-normalization was used on calibration curves (using USGS glass standards), which were linear (P1: r≥0.9903; P2: r≥0.9947), and reproducibility of replicate analyses is <6% rsd. Laser data reduction was conducted using the LasyBoy® macro (Joel Sparks, Boston University). Scanning electron microscope (SEM) images were taken using the JEOL JSM-5900LV SEM at the Engineering Department at URI. Data inspection and classifications were performed using the petrologic plotting and modeling programs Igpet © and Mixing © (Carr 2005).

Results

Whole-rock compositions

P1 samples collected during fieldwork in January 2005 consist exclusively of ashfall deposits. No bulk analysis of these samples has been carried out. Whole-rock data for P1 samples collected close to Hudson volcano are available in the literature (e.g., Bitschene et al. 1993; Ippach 2001, unpubl. PhD Thesis). The scoria from P1 is basaltic to basaltic-andesite in composition, with SiO_2 abundance ranging from 50 to 54 wt% (Table 1).

In contrast, whole-rock analyses of pumice fall samples from P2 are more evolved than P1 scoria, ranging from trachyandesite to trachydacite, occupying a narrow range in SiO_2 abundance from 60 to 62 wt% (Table 1). Results obtained as part of this study plot within a narrow field defined by >50% of the previously published data. There is a clear compositional gap (from 54 to 60 wt% SiO_2) between samples from the two phases. Although occupying narrower ranges, the major element compositions obtained from this study are similar to those reported by previous authors (60.15–64.28 wt% SiO_2; 1.27–1.59 wt% TiO_2; 1.61–2.39 wt% MgO; and 2.01–2.63 wt% K_2O). The 1991 P2 samples also show similar ranges in trace element compositions to those previously published (e.g., Naranjo and Stern 1998; Gutiérrez et al. 2005) with elevated Ba, Nb, Ce and Zr relative to other SVZ centers.

Table 1 Major and trace element bulk rock compositions of samples from P1 and P2 of the 1991 Hudson eruptions (measured by XRF), normalized to 100. Pre-recalculation LOI are also given

Sample	HUD209	HUD143	HUD208	HUD141	HUD207	HUD206	HUD210	HUD149	HUD155	190891–5	190392.3a[2]	190192.3f[3]	300192.4a[3]	100891[1]	PC-1[1]	210192.1D[2]	HUD204
Phase	2	2	2	2	2	2	2	2	2	2	2	2	2	1	1	1	3600 BP
Unit	A	A	B	B	C	C	D	D	D	-	-	-	-	-	-	-	17
Locale	28	17	28	17	28	27	28	17	17	-	-	-	-	-	-	-	17
SiO_2	61.38	61.40	61.05	61.07	60.33	60.99	62.05	61.23	61.68	62.10	61.77	61.36	61.83	51.75	51.71	51.44	65.12
TiO_2	1.29	1.29	1.32	1.32	1.38	1.31	1.24	1.31	1.29	1.36	1.32	1.36	1.30	2.13	2.36	2.15	0.91
Al_2O_3	16.69	16.45	16.77	16.66	16.74	16.70	16.39	16.73	16.43	16.38	16.44	16.39	16.43	15.88	15.85	15.79	16.87
Fe_2O_3	6.03	6.02	6.12	6.14	6.56	6.20	5.88	6.18	6.04	-	6.11	6.38	5.97	-	-	11.74	4.50
FeO	-	-								5.57				11.21	11.18		
MnO	0.18	0.18	0.18	0.18	0.18	0.18	0.17	0.18	0.18	0.18	0.19	0.18	0.18	0.19	0.19	0.19	0.14
MgO	1.73	2.07	1.80	1.74	1.94	1.83	1.70	1.75	1.70	1.74	1.69	1.72	1.70	4.32	4.28	4.21	1.22
CaO	3.72	3.65	3.81	3.83	4.12	3.94	3.74	3.72	3.61	3.69	3.60	3.77	3.53	8.33	8.25	8.24	2.39
Na_2O	6.16	6.11	6.12	6.23	5.96	6.10	5.98	6.09	6.20	6.22	6.01	5.95	6.07	4.36	4.42	4.27	5.57
K_2O	2.37	2.39	2.35	2.37	2.31	2.32	2.43	2.38	2.43	2.49	2.44	2.40	2.45	1.36	1.35	1.22	3.05
P_2O_5	0.44	0.44	0.46	0.46	0.48	0.44	0.42	0.44	0.45	0.27	0.44	0.48	0.42	0.48	0.43	0.71	0.23
Total	100	100	100	100	100	100	100	100	100	100	100	100	100	100	100	100	100
LOI	0.09	0.11	0.09	0.18	0.97	0.63	0.36	0.07	0.08	2.02	-	0.05	0.28	1.39	1.33	-	3.80
S	192	0	216	0	246	0	232	0	0	-	-						170
Sc	15.7	0	15.0	0	18.0	0	18.1	0	0	-	8	11	13			25	12
V	58.9	65.8	69.6	73.1	87.0	73.3	73.9	71.4	61.5	-	67	68	59			322	43
Cr	18.7	0	15.9	0	21.4	0.4	31.8	0	0	-	<18	<18	<18			19	14
Co	5.5	2.8	4.9	4.4	6.8	10.5	5.7	7.5	1.2	-	<4	15	6			33	0
Ni	2.0	3.1	1.6	4	2.5	4.5	1.8	3.1	2.4	-	7	6	6			12	3
Cu	5.5	7.5	7.4	5.8	8.7	7.8	6.6	5.1	4.6	-	<4	25	15			45	9
Zn	104.1	100	106.5	98	106.9	101	96.9	99.1	98.9	-	103	107	102			91	83
Ga	21.1	22.8	21.7	22.5	21.1	19.9	21.6	21.9	21.3	-	20	25	22			19	20
Rb	59.1	58.9	59.4	57.1	56.2	57.4	60.1	58.8	59.4	-	60	60	59			27	76
Sr	369.1	348.9	370.2	364.6	371.3	374.1	349.5	354.3	351.3	-	365	376	358			524	217
Y	49.8	48.9	48.5	49.1	47.4	47.9	47.1	48.5	48.7	-	47	46	46			35	54
Zr	371.2	369	367.7	359.7	361.5	354.3	380.6	363.8	367.7	-	365	353	355			178	541
Nb	21.3	18.9	20.3	18.5	20.8	18.5	20.1	18.6	18.9	-	18	16	21			5	26
Mo	-	-	-	-	-	-	-	-	-	-	5	4	<2			2	0
Cs	-	-	-	-	-	-	-	-	-	-	-	-	-			-	-
Ba	707.4	715.2	727.9	703.9	711.0	705.1	721.3	709.9	692.9	-	691	662	685			371	919
Lu	-	-	-	-	-	-	-	-	-	-	-	-	-			-	-
Hf	9.0	0	9.4	0	10.0	0	9.8	0	0	-	-	-	-			-	14
Pb	11.6	11.4	13.1	11.2	13.9	12.5	13.1	9.6	10.3	-	11	16	19		9	9	15
La	54.7	64.4	55.7	71.2	63.5	56.5	55.7	55.8	44.2	-	40	41	28		18	18	75
Ce	96.1	104.3	96.1	99.9	107.1	99.1	101.2	116.1	91.6	-	88	90	79		49	49	143
Nd	-	-	-	-	-	-	-	-	-	-	41	36	33		30	30	-
Sm	-	-	-	-	-	-	-	-	-	-	8	7	<6		9	9	0
Eu	-	-	-	-	-	-	-	-	-	-	-	-	-		-	-	-
Tb	-	-	-	-	-	-	-	-	-	-	-	-	-		-	-	-
Yb	-	-	-	-	-	-	-	-	-	-	-	-	-		-	-	0
Th	4.5	0.6	5.0	4.5	1.1	6.8	4.7	0.5	0	-	<4	<4	<4		4	4	0
U	-	-	-	-	-	0.1	-	-	-	-	<6	<6	<6		6	6	0

Data from Naranjo et al. (1993)[1], Bitschene et al. (1993)[2], and Ippach (2001)[3]

Mineralogy and petrography

P1 tephra fall is black, basaltic vitric ash that is relatively crystal poor. The ash collected at Puerto Aisén comprises tachylite (~50 vol%), pale brown, plagioclase-phyric sideromelane (~45 vol%), lithic clasts (~5 vol%) and plagioclase, clinopyroxene and Fe-Ti oxide crystals (Bitschene and Fernández 1995). Tachylitic particles are generally blocky with low vesicularity (Fig. 3a). There is a high abundance of intergrown microlites (Fig. 3b) of varying morphologies including tabular, hopper, and swallowtail. These particles also include large, ovoid vesicles (Fig. 3a). The tachylitic particles are similar to samples from the 2001 basaltic eruption of Mt. Etna (e.g., Taddeucci et al. 2004). Sideromelane fragments are brown, fluidal to irregularly shaped, and more vesicular than the tachylite (Figs. 3c & 3d). There also appears to be a smaller population of larger microlites (Fig. 3d).

The P1 phenocryst assemblage includes, in order of abundance, plagioclase (0.6–1.1 wt%), augite (~0.4 wt%), olivine (~0.4 wt%), Fe-Ti oxides (~0.2 wt%) and trace orthopyroxene (with the remaining ~98% being glass). Glass adheres to almost all crystals. Euhedral to anhedral plagioclase phenocrysts display both complex and oscillatory zoning. Several plagioclase phenocrysts show partial resorption and sieve textures. The P1 plagioclase compositions range from An_{46} to An_{80} (Table 2). Although the P1 plagioclase core compositions cover a large range (An_{30} to An_{87}), the most common occurs at approximately An_{75} (Fig. 4a). P1 plagioclase rims occupy a narrower compositional range (An_{46} to An_{77}) with most of the data clustered around An_{58} and An_{75}.

Clinopyroxene and olivine phenocrysts in P1 samples are typically euhedral to subhedral. The compositional ranges occupied by both augite (Wo_{44-45}) and olivine ($Fo_{\sim68}$) phenocrysts are narrow (Table 3). Most grains are relatively homogeneous, with no core-to-rim variations. In general, Fe-Ti oxides are subhedral to anhedral with embayed margins and some are highly fractured. No core-to-rim compositional variations were identified within the oxides (Table 3). The lack of zonation may indicate that the oxides were in equilibrium with the melt prior to eruption.

Tephra fall deposits from P2 display sharp contacts between alternating units of pale gray fine ash, and gray coarse lapilli. The pale gray units are composed of glass shards, pumice, crystal and lithic fragments (Scasso et al. 1994). Glassy pyroclasts range from pale gray/white tube pumice to dark brown/black, blocky, poorly vesicular shards (Fig. 3e) (Scasso and Carey 2005). The P2 pumice samples collected for our study are highly vesicular (Fig. 3f) and vary from dark gray/black to pale brown/tan. Several reworked samples collected from Lago Buenos Aires display prominent color bands (Fig. 5a).

Plagioclase is the dominant phenocryst phase in the P2 products (6.1–7.7 wt%), with augite (0.4–1.3 wt%), olivine (0.1–0.7 wt%), Fe-Ti oxide (1.1–1.9 wt%) phenocrysts and apatite (~0.1 wt%) present in smaller quantities (the remainder being glass). This assemblage occurs as either single phenocrysts or glomerocrysts. Euhedral to anhedral and broken plagioclase with complex and oscillatory zoning are common. Evidence of partial resorption (e.g., embayed margins) is visible in some phenocrysts. Plagioclase compositions range from An_{28} to An_{83} (Table 2). The majority of both rim and core compositions cluster around An_{43} (Fig. 4b).

Clinopyroxene (Wo_{44-45}) and olivine ($Fo_{\sim68}$) phenocrysts within P2 trachyandesite pumice are relatively homogeneous, with little core-to-rim variation. Most are subhedral to anhedral and broken, and highly fractured with round edges, and contain Fe-Ti oxide and apatite inclusions (Table 3). All hand-picked phenocrysts have adhering glass. In general, the Fe-Ti oxides are subhedral to anhedral and occur as clusters of large magnetite and smaller ilmenite crystals (Table 3). Embayed margins and rounded edges are present (Fig. 3f) and several examples are highly fractured.

Groundmass glass compositions

P1 glass consists of medium-brown transparent shards and microlite-rich tachylitic clasts, and encompasses a narrow range in composition from basalt to basaltic trachyandesite (Fig. 6; Table 4). The glass compositions are similar to the bulk rock compositions, reflecting the generally crystal-poor nature of the magma.

P2 glasses are more diverse in composition ranging from trachyandesite to trachydacite (Fig. 6; Table 4). The analyzed glass samples occupy a broader SiO_2 range (60–65 wt%) than the bulk rock analyses (60–62 wt%). The glass compositions decrease in SiO_2 from the earliest part (unit A) to the final part (unit D) of the P2 eruption (Fig. 7). Although the overall SiO_2 content of the different units (A, B, C, D) changes, the most commonly occurring melt composition, as represented by unit B, is present in each unit (Fig. 7). The trend of decreasing SiO_2 content during the eruption is thus reflected in the total compositional range of the groundmass glasses, which increases from unit A to D. The existing bulk rock compositions show only a very slight trend towards more mafic compositions in units A to D (Table 1).

Gray and black banded pumice clasts from the P2 eruption have been previously described as mixtures of rhyolitic and trachyandesitic compositions (e.g., Bitschene and Fernández 1995). However, our analyses of P2 pumice glass did not yield rhyolitic compositions.

Rare-earth element plots for glasses from both phases of the 1991 eruption have similar, LREE-enriched trends, and
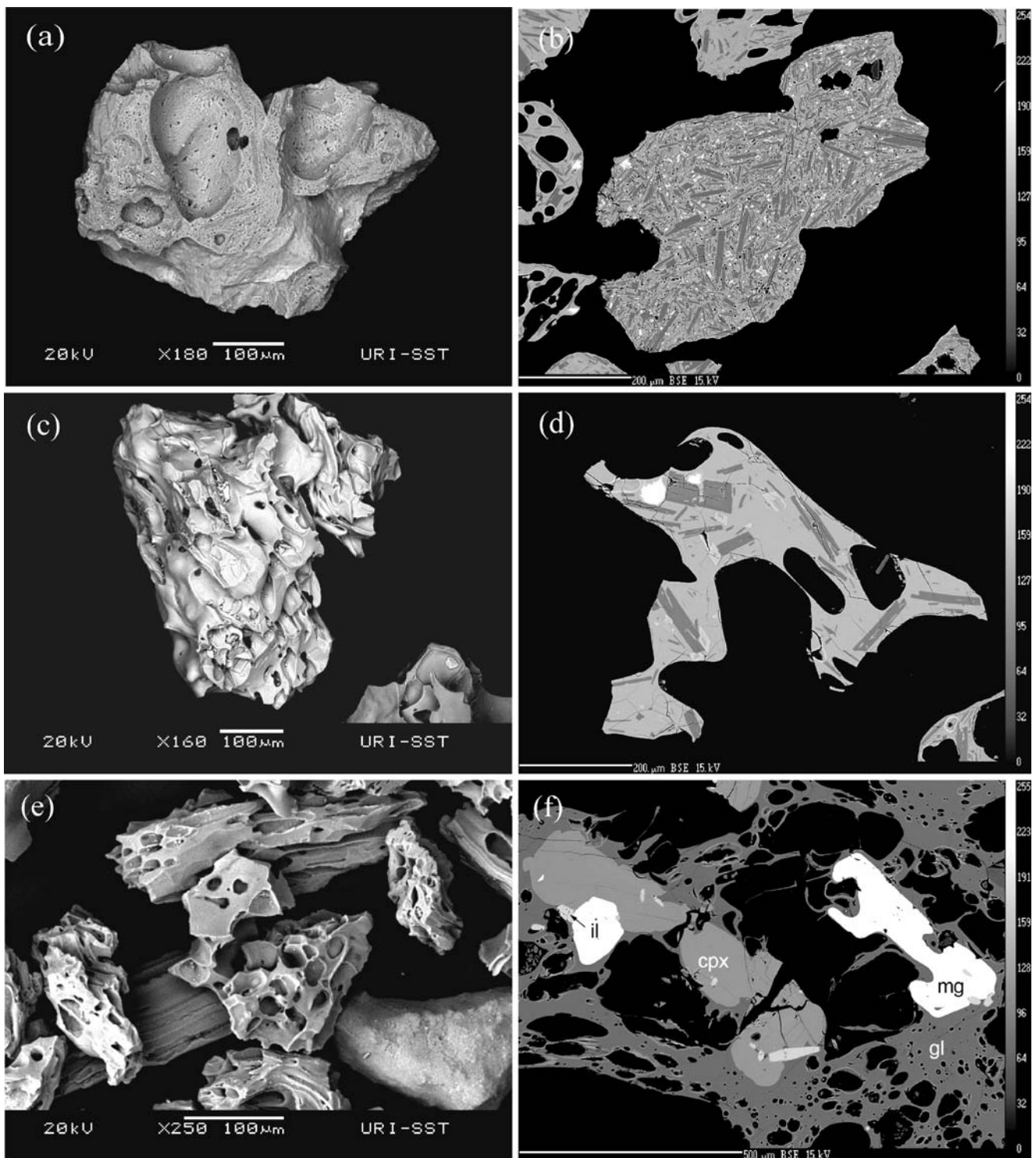
Fig. 3 Scanning electron microscope (SEM, *left column*) and back-scattered electron (BSE, *right column*) images of juvenile pyroclasts from both phases of the 1991 Hudson eruption. **a** and **b**: blocky, microlite-rich juvenile pyroclasts from P1. **c** and **d**: vesicular, fluidal, moderately microlitic sideromelane from P1. **e** and **f**: vesicular, microlite-poor, porphyritic glass shards from P2. Representative phenocryst assemblages are shown in image **f** from unit A: *mg* - magnetite; *il* - ilmenite; *gl* - glass; *cpx* – clinopyroxene; plagioclase absent

Table 2 Representative electron microprobe analyses of plagioclase phenocrysts from P1 and P2 of the 1991 Hudson eruptions

Phase	Unit	Sample	SiO$_2$	Al$_2$O$_3$	FeO	CaO	Na$_2$O	K2O	Total	An	Ab	Or	Location
P1		HUD110	51.27	31.15	0.63	13.87	3.44	0.12	100.48	68.8	29.1	0.7	rim
		HUD110	47.41	33.6	0.53	17.16	1.84	0.05	100.59	83.3	15.0	0.3	core
		HUD110	53.45	29.00	0.85	11.83	4.41	0.2	99.75	58.7	37.3	1.2	rim
		HUD110	61.00	24.84	0.33	6.26	7.36	0.52	100.3	31.1	62.3	3.1	core
P2	A	HUD209	57.56	26.83	0.54	8.68	5.99	0.32	99.93	43.1	50.7	1.9	rim
		HUD209	59.16	25.85	0.44	7.51	6.56	0.39	99.9	37.3	55.5	2.3	core
	B	HUD208	57.44	27.16	0.54	8.88	5.95	0.31	100.27	44.1	50.4	1.8	rim
		HUD208	57.59	26.58	0.43	8.53	6.09	0.33	99.55	42.3	51.5	2.0	core
	C	HUD207	57.25	27.12	0.56	9.41	5.66	0.3	100.31	46.7	47.9	1.8	rim
		HUD207	55.95	28.16	0.53	10.2	5.32	0.25	100.41	50.6	45.0	1.5	core
	D	HUD210	54.97	28.34	0.91	11.15	4.8	0.22	100.39	55.1	40.6	1.3	rim
		HUD210	47.46	33.51	0.54	17.01	1.86	0.05	100.42	82.9	15.6	0.3	core

the P2 concentrations are generally elevated relative to P1 (Fig. 8a). There is an overall decreasing trend from LREE to HREE in both phases and P2 exhibits a slightly steeper LREE slope than P1. Negative Eu anomalies are present in both the P1 and P2 REE patterns and represent varying degrees of plagioclase fractionation. The anomaly is more pronounced in P2 than in P1 and reflects the greater crystallinity seen in the P2 samples (~9–11% versus ~2%). The tight clusters of select trace element ratios in both P1 and P2 samples suggests crystal fractionation processes occurred during the formation of these source magmas (Fig. 8b). The REE patterns are consistent with previously published work (e.g., Gutiérrez et al. 2005). Both P1 and P2 samples show a negative Nb anomaly typical of subduction zone environments (Wilson 1989) when plotted on a Rock/MORB normalized 'spider' diagram (not shown).

Melt inclusion compositions

Pale gray to dark brown glassy melt inclusions are common in both plagioclase and pyroxene phenocrysts from the P1 tephra fall deposits. The inclusions encompass a narrow compositional range (53 to 57 wt% SiO$_2$), and are typically more evolved than the co-existing groundmass glasses (Fig. 6; Table 5).

Plagioclase- and pyroxene-hosted, pale to dark brown glass inclusions are also common in P2 samples. There are no significant compositional differences evident between inclusions hosted in plagioclase, versus pyroxene. The inclusions encompass a compositional range that is narrower than the groundmass glasses (62–65 wt% SiO$_2$; Fig. 6; Table 5). In general, the inclusions are either similar to, or more evolved than, the co-existing groundmass glass of the sample. There appears to be a trend where the range of the analyzed groundmass glass extends to more mafic compositions relative to the melt inclusions as the eruption pro-
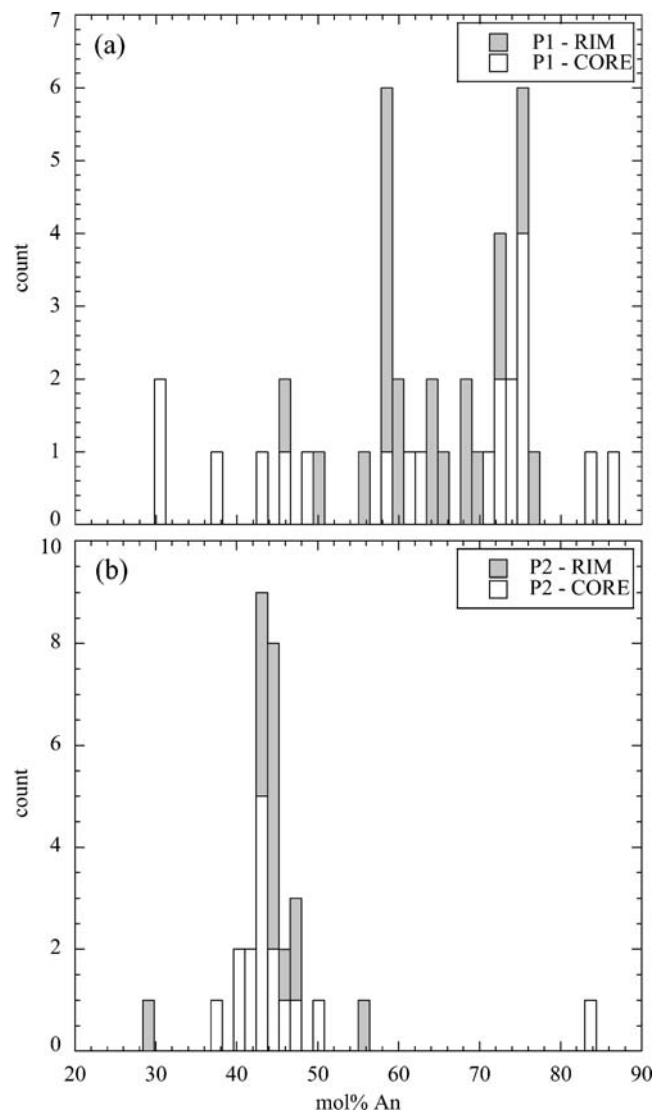

Fig. 4 Histograms showing the distribution of anorthite values for plagioclase phenocrysts from the 1991 eruptions. **a** P1 rim and core compositions from ~20 phenocrysts taken from two samples (HUD110–2 & HUD110–3). **b** P2 rim and core compositions from ~15 phenocrysts taken from all units A-D (4, 3, 4, 4 respectively)

Table 3 Representative electron microprobe analyses of pyroxene and olivine phenocrysts and Fe-Ti oxides pairs from both phases of the 1991 Hudson eruptions

	Sample		SiO$_2$	TiO$_2$	Al$_2$O$_3$	FeO	MnO	MgO	CaO	Na$_2$O	K$_2$O	Cr$_2$O$_3$	Total	En	Wo	Fs	Fo	Fa
	Ferromagnesian minerals																	
P1	HUD110C-2	cpx	51.53	0.84	2.25	7.71	0.36	15.79	20.37	0.33	0.00	0.001	99.19	45.44	42.11	12.45	-	-
	HUD110C-4	cpx	49.46	1.13	3.74	7.85	0.21	15.09	20.41	0.36	0.01	0.125	98.40	44.17	42.94	12.89	-	-
	HUD110C-5	ol	36.15	0.05	0.01	27.59	1.02	33.35	0.20	0.01	0.01	0.002	98.39	-	-	-	68.30	31.70
P2-A	HUD209B-1	cpx	51.58	0.79	2.08	8.68	0.55	15.44	20.21	0.44	0.01	0.007	99.78	44.32	41.70	13.98	-	-
	HUD209B-2	ol	37.32	0.04	0.04	27.72	1.04	33.68	0.17	0.02	0.01	0.020	100.1	-	-	-	68.41	31.59
P2-B	HUD208A-1	cpx	51.77	0.74	1.91	8.79	0.62	15.29	20.09	0.46	0.00	0.000	99.22	44.11	41.67	14.22	-	-
	HUD208A-3	ol	37.25	0.02	0.01	27.79	1.09	33.29	0.16	0.01	0.01	0.000	99.63	-	-	-	68.11	31.89
P2-C	HUD207D-1	cpx	51.96	0.77	1.91	8.65	0.61	15.29	20.29	0.43	0.00	0.001	99.91	44.04	41.99	13.97	-	-
	HUD207C-3	ol	37.10	0.02	0.02	27.39	1.04	33.36	0.16	0.00	0.01	0.002	99.09	-	-	-	68.47	31.53
P2-D	HUD210A-1	cpx	50.71	0.97	2.66	8.79	0.58	15.13	19.79	0.42	0.01	0.008	99.07	44.12	41.49	14.39	-	-
	HUD210A-3	ol	37.03	0.04	0.03	27.62	1.05	33.55	0.14	0.02	0.04	0.014	99.53	-	-	-	68.40	31.60
	Fe-Ti Oxides													*mol% Usp*			*Mol% Ilm*	
P1	HUD110 pair-1			19.18	1.54	71.94	0.58	0.75				0.086	94.07	43.90				
	HUD110 pair-1			49.47	0.10	45.25	0.80	1.47				0.008	97.10				86.70	
P2-A	HUD209 pair-2			15.65	2.79	72.41	0.86	3.75				0.022	95.49	44.30				
	HUD209 pair-2			44.80	0.34	45.23	0.93	5.28				0.009	96.59				82.00	
P2-B	HUD208 pair-2			15.79	2.89	72.10	0.79	3.80				0.025	95.40	45.20				
	HUD208 pair-2			45.24	0.34	45.25	0.88	4.73				0.011	96.45				83.00	
P2-C	HUD207 pair-1			15.68	2.79	72.28	0.82	3.75				0.020	95.34	44.50				
	HUD207 pair-1			45.23	0.36	45.23	0.82	5.26				0.015	96.91				82.70	
P2-D	HUD210 pair-2			15.63	2.74	72.37	0.87	3.79				0.014	95.42	44.10				
	HUD210 pair-2			45.05	0.39	45.21	0.86	4.95				0.010	96.47				83.10	

En: Enstatite; *Wo*: Wollastonite; *Fs*: Ferrosilite; *Fo*: Forsterite; *Fa*: Fayalite; *mol%*: mole percent; *Usp*: Ulvöspinel; *Ilm*: Ilmenite
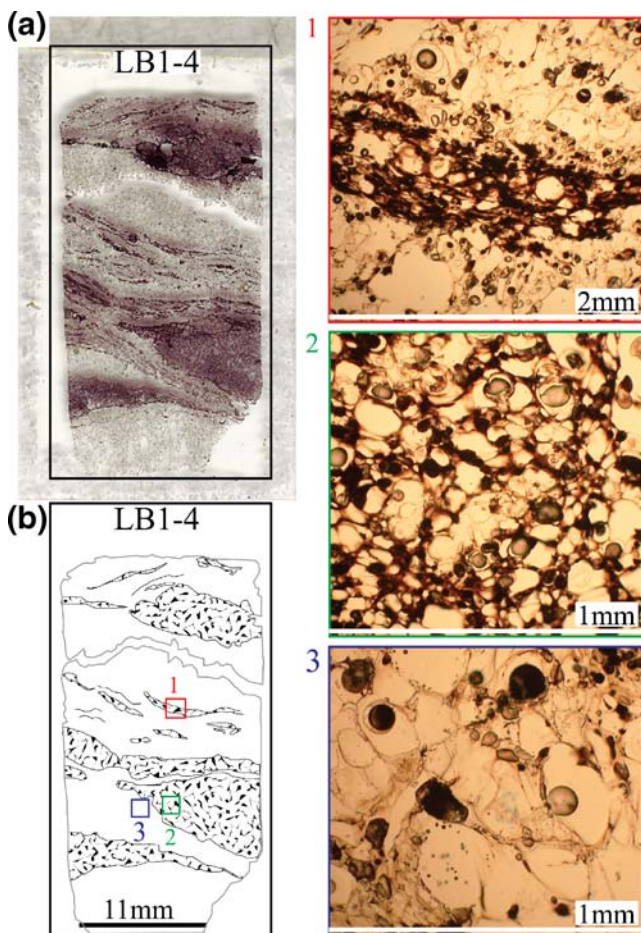
Fig. 5 a Scanned thin-section of reworked banded pumice lapilli collected from Lago Buenos Aires, approximately 130 km from Hudson volcano. b Sketch of the thin-section above showing the black (*stippled*) and gray (*open*) regions. *1*: Photomicrograph showing the contrast between *black and gray regions* (field of view (FOV) ~2 mm); *2*: Photomicrograph of vesicles and thick glass walls within the *black bands* (FOV ~1 mm); *3*: Photomicrograph showing a smaller population of larger vesicles with thinner glass walls within the *gray bands* (FOV ~1 mm)

gressed (Fig. 9). In unit A there is little difference between groundmass glasses and inclusions and the compositional spread is narrow. Units B and C exhibit more diversity in groundmass glass compositions relative to the melt inclusions. Unit D shows a marked difference, the host groundmass glass being consistently more mafic than the melt inclusions (Fig. 9).

Discussion

Evidence for magma mingling and mixing

Pumice lapilli from the P2 eruption, collected from Lago Buenos Aires, commonly exhibit distinctive black and gray bands of glass and have been previously cited as evidence

for magma mingling (e.g., Bitschene and Fernández 1995). Analysis of the gray and black bands reveals similar major element compositions and does not support physical mingling between magmas of different compositions. We attribute these color differences largely to variations in the extent of vesiculation (Fig. 5). A similar interpretation was reached for banded pumice clasts from Damavand volcano in Iran (e.g., Davidson et al. 2004). Differences in vesicularity might be due to mingling of magma of similar composition but with different volatile contents.

Other examples of mingling have been found in dark pumice fragments in unit D of the P2 fall deposits. These clasts have domains of microlite-rich glass in sharp contact with microlite-poor, brown transparent glass (Fig. 10). Microlite-rich domains may represent magma that degassed prior to the eruption and may have been syn-eruptively mixed with relatively un-degassed magma. Similar micro-scale evidence of magma mingling has been identified previously at Hudson (e.g., Gutiérrez et al. 2005) and at Stromboli volcano in Italy (e.g., Lautze and Houghton 2005).

Evidence for phenocryst-melt disequilibrium is commonly present in the phenocrysts found in deposits from both phases of the 1991 eruption. Plagioclase phenocrysts display complex and oscillatory zoning, and several examples of reverse zoning are evident in phase 2. Euhedral and subhedral phenocrysts have rounded corners, embayed areas, and sieve textures, which may represent resorption during periods of rapidly changing melt conditions. These textures combined are indicative of disequilibrium during the history of phenocryst growth and may be the result of changes in temperature, magma composition, and/or volatile content. Such changes are often associated with magma mixing (e.g., Tepley et al. 2000; Izbekov et al. 2002; Martel et al. 2006).

A small (<1 mm) plagioclase phenocryst in the basaltic scoria from P1 contains a more sodic core (An_{31}), a dissolution zone, and a more calcic rim (An_{58}). This phenocryst could be a xenocryst incorporated from the surrounding granite and partially assimilated (dissolution zone) by the rising P1 mafic magma. The rim composition (An_{58}) represents post-assimilation crystal growth. Alternatively, this may be an antecryst (e.g., Davidson et al. 2007), having initially equilibrated in a more evolved melt (core composition), encountered changing melt conditions (resorption textures), before continuing growth in a hybridized, slightly more mafic melt (resulting from magma mixing). Several P1 plagioclase phenocrysts plot within the range of compositions that are representative of the P2 plagioclase phenocrysts. Based on the combined mineralogical and melt inclusion data we interpret these phenocrysts as antecrystic in origin, having been incorporated via mingling of basaltic (P1) and trachyandesitic (P2) magmas
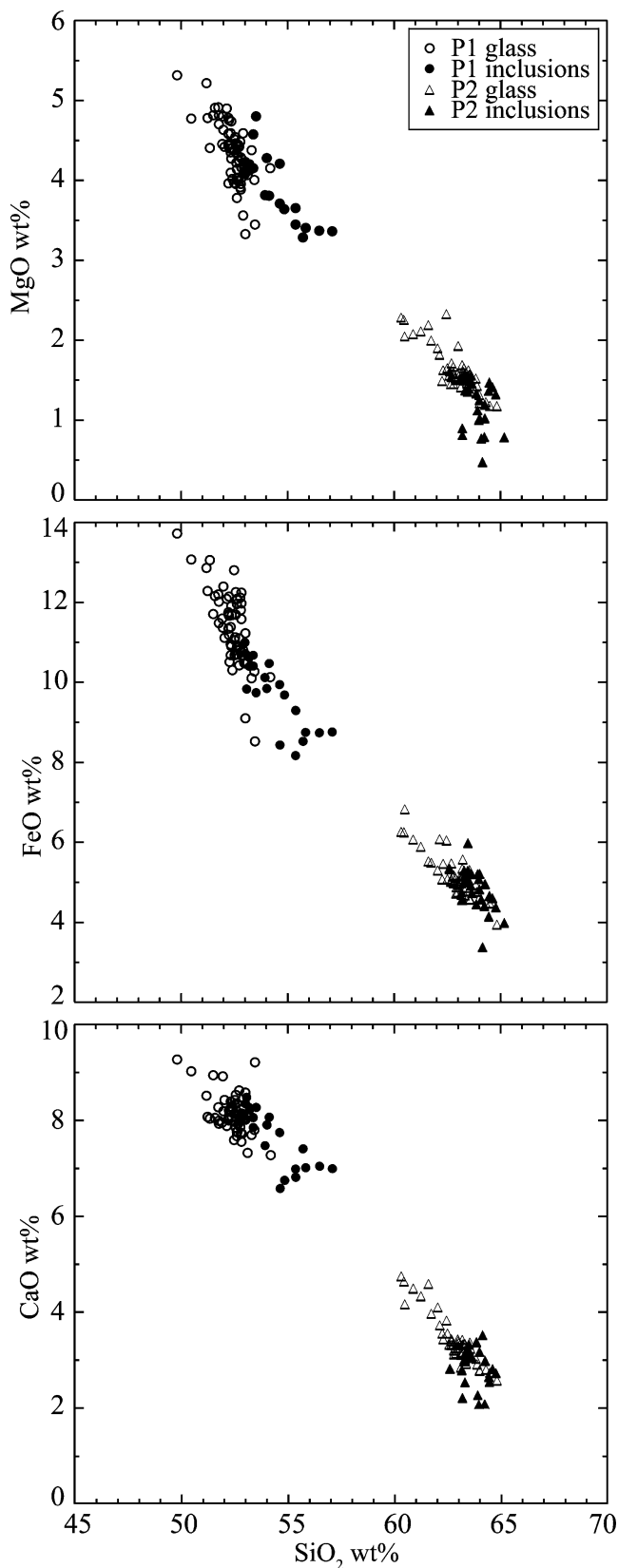
Fig. 6 Representative major element variation diagrams of ground-mass glass and melt inclusion compositions of samples from P1 and P2. *Open circles* (P1, number of analyses (n)=65) and *open triangles* (P2, n=54) represent groundmass glass samples, and *solid circles* (P1, n=22) and *solid triangles* (P2, n=29) represent melt inclusions. Note the compositional gap between ~57 to ~60 wt% SiO_2. Additional major element data are available in Tables 4 and 5

prior to eruption. In addition, a P2 pumice clast was found to contain a highly calcic (An_{83}) plagioclase phenocryst that is more typically associated with basaltic compositions and is also interpreted as an antecryst. There is thus both groundmass and phenocryst evidence for magma mixing in the products of each phase of the 1991 Hudson eruption.

An additional important piece of evidence for magma mixing is the common occurrence of plagioclase- and pyroxene-hosted melt inclusions that are significantly more evolved than the surrounding groundmass glass in samples from both the P1 and P2 eruptions (Fig. 6). Post-entrapment crystallization cannot explain these relationships as the trends in several elements, in particular FeO, are opposite to those expected from extraction of the host phase from a trapped aliquot of melt. The melt inclusion/ groundmass glass trends exhibited in Fig. 9 can thus be interpreted as an increasing extent of hybridization of P2 magma by a more mafic end member (i.e., via magma mixing).

Magma relationships

Naranjo et al. (1993) suggested that the P1 basalt intersected the lower part of a compositionally stratified chamber that fed the P2 trachyandesite eruption. Our new data confirm the existence of compositional zonation in the P2 deposits but this deposit-zonation does not necessarily translate to a simple compositionally zoned chamber prior to eruption, as there is also evidence of mingling-mixing between the P1 and P2 magmas. Furthermore, the compositionally distinct magmas of P1 and P2 could be genetically related, given that they were erupted during the same event. If related, then fractional crystallization or magma mixing could explain the compositional variations within the erupted products from the different eruptive phases (P1 and P2). We have examined potential genetic relationships using geochemical modeling of major and trace element compositions of selected end members. Liquid compositions of the 1991 magmas were selected from glasses, and fractionating phases were derived from microprobe analysis of phenocrysts in P1 and P2. A potential mixing component considered in the analysis is dacitic magma from the last major explosive of Hudson at 3,600 yrs BP (Tables 1 and 4).

There are at least three possible genetic relationships between P1 and P2 magmas; a) fractional crystallization of a basaltic magma (P1) to yield the dominant trachyandesite

Table 4 Averaged glass compositions from both phases of the 1991 and the 3,600 yrs BP Hudson eruptions as measured by electron microprobe

P1				P2 - unit A		
Sample	HUD110 Trans	HUD110 Trans	HUD110 Trans	HUD110 Tachy	HUD209 Trans	HUD209 Trans	HUD209 Trans
SiO_2	52.55 (0.15)	52.52 (0.23)	51.68 (0.19)	52.27 (0.32)	62.76 (0.30)	64.14 (0.15)	64.10 (1.01)
TiO_2	2.58 (0.03)	2.22 (0.08)	2.33 (0.03)	2.23 (0.16)	1.22 (0.07)	1.04 (0.05)	1.09 (0.04)
Al_2O_3	13.93 (0.14)	15.79 (0.20)	15.47 (0.25)	15.18 (0.58)	16.10 (0.18)	16.34 (0.08)	16.33 (0.03)
FeO	12.16 (0.37)	10.72 (0.15)	11.33 (0.12)	10.88 (0.68)	4.69 (0.19)	4.50 (0.09)	4.59 (0.55)
MnO	0.23 (0.08)	0.20 (0.07)	0.17 (0.01)	0.13 (0.03)	0.18 (0.05)	0.19 (0.06)	0.21 (0.06)
MgO	3.99 (0.08)	4.28 (0.12)	4.46 (0.10)	4.39 (0.44)	1.52 (0.02)	1.23 (0.06)	1.41 (0.20)
CaO	7.72 (0.09)	8.20 (0.15)	8.41 (0.17)	8.27 (0.64)	3.24 (0.08)	2.78 (0.03)	2.91 (0.28)
Na_2O	4.24 (0.16)	4.28 (0.23)	3.93 (0.07)	4.12 (0.14)	6.70 (0.27)	6.80 (0.31)	6.68 (0.22)
K_2O	1.45 (0.06)	1.23 (0.08)	1.30 (0.01)	1.22 (0.22)	2.57 (0.13)	2.60 (0.09)	2.68 (0.06)
P_2O_5	0.88 (0.05)	0.70 (0.07)	0.93 (0.01)	0.78 (0.04)	0.35 (0.04)	0.28 (0.03)	0.35 (0.04)
Total	99.72 (0.38)	100.15 (0.16)	99.07 (0.01)	99.47 (0.93)	99.33 (0.32)	99.63 (0.51)	100.01 (0.33)
n =	6	5	3	3	8	4	3

P2 - unit B			P2 - unit C	P2 - unit D		3600	
Sample	HUD208 Trans	HUD208 Trans	HUD207 Trans	HUD210 Trans	HUD210 Tachy	HUD204 Trans	HUD203 Trans
SiO_2	62.23 (0.35)	63.06 (0.46)	61.59 (0.96)	62.42 (0.47)	60.84 (0.39)	68.49 (0.30)	67.23 (0.39)
TiO_2	1.21 (0.09)	1.20 (0.09)	1.31 (0.07)	1.27 (0.06)	1.47 (0.02)	0.68 (0.02)	0.63 (0.06)
Al_2O_3	16.18 (0.20)	16.20 (0.05)	16.01 (0.08)	15.97 (0.13)	15.75 (0.21)	15.34 (0.08)	15.11 (0.21)
FeO	4.94 (0.16)	4.99 (0.10)	5.49 (0.49)	5.23 (0.08)	6.18 (0.48)	3.05 (0.11)	3.00 (0.28)
MnO	0.18 (0.07)	0.18 (0.05)	0.23 (0.05)	0.15 (0.05)	0.22 (0.03)	0.11 (0.04)	0.14 (0.03)
MgO	1.58 (0.07)	1.45 (0.06)	1.93 (0.24)	1.64 (0.15)	2.15 (0.10)	0.64 (0.04)	0.62 (0.02)
CaO	3.32 (0.17)	3.22 (0.26)	3.85 (0.54)	3.41 (0.41)	4.50 (0.21)	1.67 (0.02)	1.55 (0.05)
Na_2O	6.64 (0.16)	6.74 (0.26)	6.31 (0.45)	6.16 (0.23)	6.15 (0.08)	6.49 (0.12)	6.44 (0.26)
K_2O	2.40 (0.06)	2.62 (0.06)	2.35 (0.11)	2.99 (0.38)	2.18 (0.15)	3.48 (0.10)	3.43 (0.11)
P_2O_5	0.36 (0.06)	0.39 (0.02)	0.43 (0.03)	0.42 (0.09)	0.58 (0.04)	0.12 (0.04)	0.10 (0.02)
Total	99.04 (0.52)	99.67 (0.13)	99.13 (0.35)	99.25 (0.41)	99.44 (0.30)	100.07 (0.52)	98.24 (0.72)
n =	5	3	6	4	4	5	6

One standard deviation shown in parentheses.

n = number of analyses; trans: translucent; tachy: tachylite.

magma (P2) (i.e., unit B), b) mixing of P1 basaltic magma with the volumetrically dominant trachyandesite to yield more mafic trachyandesite found in the upper units of the P2 fall sequence (C and D), or c) mixing of P1 basaltic magma with a more evolved dacitic magma to yield the dominant P2 trachyandesite composition (Fig. 11). Generation of the P2 trachyandesite from the P1 basalt by fractional crystallization and/or magma mixing has been evaluated using both the least and most evolved P1 glass compositions as possible parental magmas (Fig. 11a). Results from major and trace element modeling indicate that both starting compositions can fractionally crystallize plagioclase (7.8–18.0%), clinopyroxene (4.8–11.6%), orthopyroxene (1.9–6.9%), magnetite (2.9–6.7%) and apatite (0.5–1.5%) to produce the dominant trachyandesite composition of P2 unit B (62.9 wt% SiO_2). The sum of squares of residuals (SSR) from this modeling ranges from 0.063 to 0.093, indicating a very good fit to the data. In addition, mixing between an average P1 composition (~9% by volume) and P2 unit B (~91% by volume) can produce more mafic trachyandesite similar to P2 unit C composition with similarly low sum of squares of residuals (SSR 0.055). The geochemical modeling does not support the possibility that the dominant P2 trachyandesite is the product of mixing between a residual dacite from the 3,600 yrs BP explosive eruption and the P1 basalt (SSR 0.9–1.0). These results do not necessarily prove specific genetic links, rather they demonstrate that basaltic magmas produced by Hudson can undergo fractionation or mixing to produce trachyandesite compositions similar to that erupted during P2. Although the modeling suggests that the compositionally distinct magmas of P1 and P2 can be related through fractional crystallization, the melt inclusion data (i.e., typically more evolved compositions than coexisting groundmass glass), the inferred extent of mixing (i.e., units B, C & D; Fig. 9), and the general straight-line trends of the major element data confirm the important role of magma mixing during the 1991 eruptions.
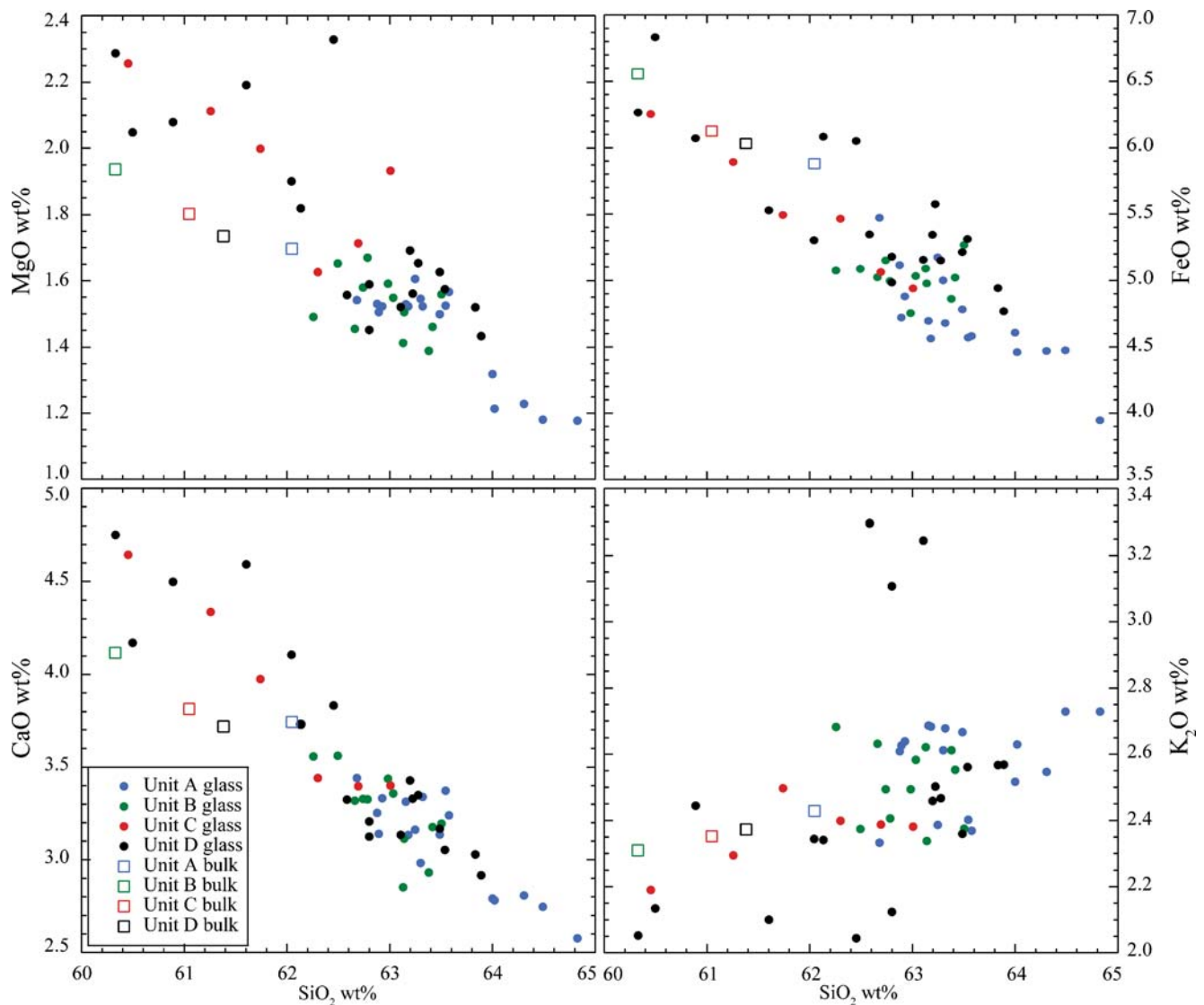
Fig. 7 Major element variation diagrams of groundmass glass (*filled circles*) and bulk rock (*open squares*) compositions of subunits in the P2 fall deposit. Note the trend of decreasing SiO₂ from the earliest part (unit A) to the final part of the eruption (unit D). 53 glass analyses total from all four units (A, *n*=17; B, *n*=12; C, *n*=6; D, *n*=18)

We now further consider the compositional diversity exhibited by P1 and P2 eruptive products (Fig. 6). Variations within the P1 samples can be reproduced by both mixing and fractional crystallization (Fig. 11b). Geochemical modeling indicates the least evolved P1 composition (50.93 wt% SiO₂) can produce the most evolved P1 glass composition by fractionation of plagioclase, clinopyroxene, magnetite, and trace olivine and apatite (SSR 0.11). Alternatively, mixing between the least evolved P1 glass composition (50.93 wt% SiO₂) and the most evolved P1 glass composition (54.19 wt% SiO₂) can also produce an average P1 composition (51.93 wt% SiO₂), returning relatively low SSR values of ~0.2. The melt inclusion and plagioclase rim and core data (i.e., generally more evolved than coexisting groundmass glass (Fig. 6)

and inferred antecryst origins (Fig. 4) respectively) suggest magma mixing played a dominant role. However, it is possible that both fractional crystallization and magma mixing were operating in concert to produce the observed compositional diversity in P1.

Compositional variations within the P2 eruptive products can also be explained through a combination of fractional crystallization and magma mixing (Fig. 11c). As mentioned previously, an average P1 basaltic composition can be mixed with a P2 unit B trachyandesite composition to produce the more mafic trachyandesite found in P2 unit C (SSR 0.03–0.09). Fractionation of P2 unit B trachyandesite involving clinopyroxene, magnetite and apatite (with trace ilmenite and olivine) can produce the more evolved P2 trachyandesite compositions found in unit A (SSR 0.13).
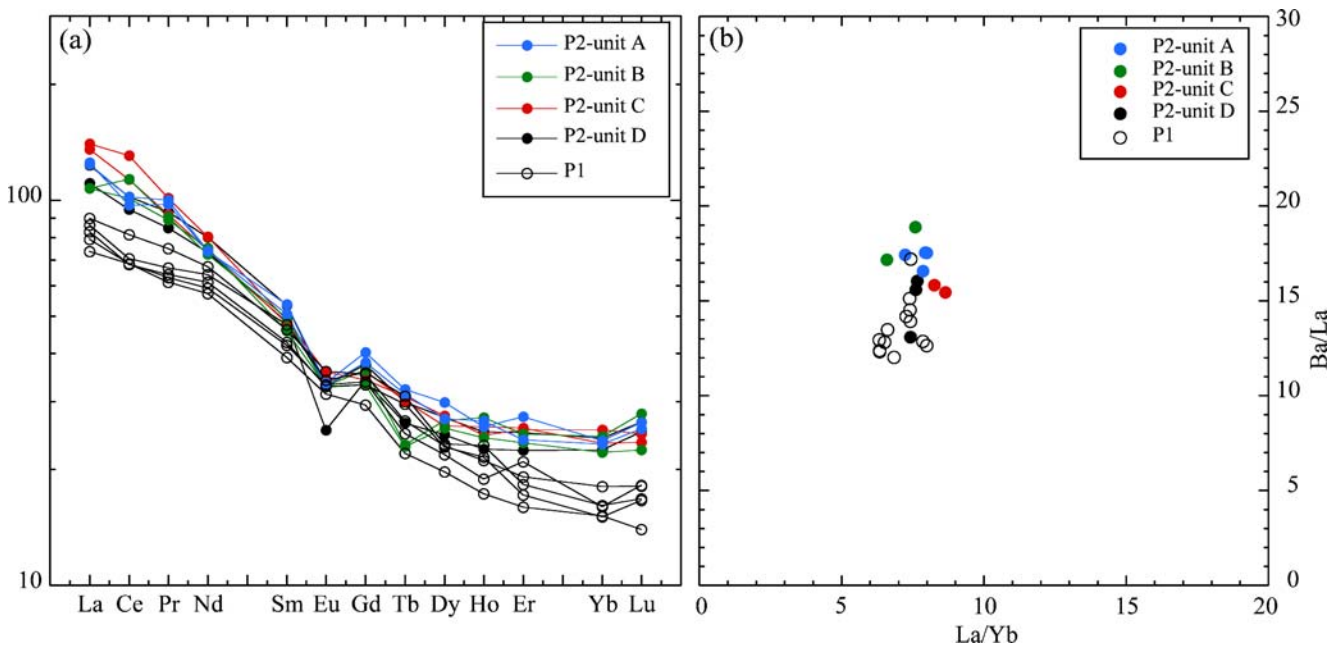
Fig. 8 a REE plot for P1 (*open circles*) and P2 (*solid circles*) groundmass glasses. An overall LREE-enriched trend and negative Eu anomaly are visible in both the P1 and P2 patterns. **b** Ba/La versus La/Yb variation diagram for P1 and P2 glasses. Note the tight clustering of select trace element ratios, suggestive of fractional crystallization

Alternatively, the most evolved P2 glass composition can also be produced through fractional crystallization (~12–18%) of the least evolved P2 trachyandesite composition involving plagioclase (~8%), clinopyroxene (~5%), magnetite (~3%), orthopyroxene (~2%) and <1% apatite (SSR 0.03–0.10). However, the typically more evolved melt inclusions relative to groundmass glass in many of the P2 samples favor magma mixing in the latter part of the P2 eruption.

In summary, the geochemical modeling suggests that magmas erupted during phases 1 and 2 of the 1991 Hudson eruption can be related through both magma mixing and fractional crystallization processes. Trachyandesite from unit B is the most commonly occurring composition within the P2 products, having been erupted throughout the event, and is likely to be the result of fractionation of a basaltic magma similar in composition to melts erupted during P1. Variations towards more mafic compositions within P2 can be produced through mixing between basaltic melts from P1 and the volumetrically dominant trachyandesite of unit B, P2 (Fig. 11a). More evolved melts within P2 (Fig. 11c) can be produced through fractionation of clinopyroxene, magnetite and apatite with trace olivine and ilmenite from trachyandesite of unit B composition.

Pre-eruptive conditions of the 1991 Hudson magmas

Geothermometry, volatile contents, inferred pressures, and comparisons with experimental studies are used here to define the nature of the pre-eruptive magmatic system

beneath Hudson. Previous studies have dealt with magma genesis at depth (e.g., Bitschene and Fernández 1995; Gutiérrez et al. 2005) without speculating on the nature or location of shallow crustal reservoirs.

Temperatures

Equilibrium temperatures and oxygen fugacities of the P1 (basaltic) and P2 (trachyandesitic) magmas have been estimated from two-oxide geothermometry using the QUILF program (Andersen et al. 1993; Andersen and Lindsley 1988). Only coexisting Fe-Ti oxide pairs from P2 satisfied the Bacon and Hirschmann (1988) Mg/Mn equilibrium test. Phenocryst-melt disequilibrium is reflected in the failure of P1 oxide pairs to pass the Mg/Mn equilibrium test. Given the comparatively fast speeds (i.e., days to months) at which coexisting Fe-Ti oxide minerals re-equilibrate (e.g., Venezky and Rutherford 1999) a relatively recent mixing event and subsequent pre-eruptive cooling could explain this disequilibrium.

Phase 1 temperatures ranged from 927 to 943±27°C for analyses of nine magnetite-ilmenite pairs, although one anomalously low temperature (796±26°C) was recorded. All the Fe-Ti oxide pairs from P1 failed the Bacon and Hirschmann (1988) Mg/Mn equilibrium test, therefore we have used the mineral phase assemblages, the degree of crystallization, and the water content in glasses from the experimental work of Moore and Carmichael (1998) to tentatively constrain the P1 pre-eruption temperature

Table 5 Major and select trace element compositions of melt inclusions from P1 and P2 of the 1991 Hudson eruptions as measured by electron microprobe and ICP-MS

Phase	1	1	1	1	1	1	2	2	2	2	2	2	2	2	2	2
Unit	-	-	-	-	-	-	A	A	B	B	C	C	C	C	D	D
sample	110–3	110–3	110–3	110–3	110–2	110–2	209	209	208a	208a	207a	207b	207b	207b	210a	210B
Inclusion	#3	#4	#5	#3a	#3	#1	#3	#2	#5	#1	#1	#2c	#3c	#4	#2	#3
SiO_2	57.06	53.62	54.54	60.71	52.05	51.81	61.20	61.89	61.90	63.21	62.76	62.76	61.61	62.79	61.35	62.67
TiO_2	1.91	2.13	2.15	1.46	2.09	2.11	1.15	1.17	1.00	0.99	1.28	1.28	1.22	1.19	1.09	1.06
Al_2O_3	16.90	16.49	16.78	16.66	15.89	15.96	15.40	16.09	15.76	16.09	16.33	16.33	15.85	15.52	16.40	16.16
FeO	8.75	10.06	10.55	7.06	10.80	10.47	5.77	4.60	5.44	4.33	5.08	5.08	4.64	4.04	4.52	4.50
MnO	0.16	0.24	0.22	0.17	0.18	0.20	0.22	0.16	0.21	0.19	0.23	0.23	0.20	0.19	0.18	0.17
MgO	3.36	3.79	3.83	2.09	4.00	4.01	1.45	1.43	1.33	1.32	1.57	1.57	1.48	1.33	1.34	1.31
CaO	6.99	7.43	8.12	5.13	8.20	8.16	3.11	2.96	3.04	2.78	3.30	3.30	2.73	2.58	2.60	2.87
Na_2O	2.82	3.67	2.65	2.98	3.01	2.95	6.10	5.97	6.12	6.43	6.30	6.30	6.54	6.64	6.35	6.45
K_2O	0.97	0.95	1.00	1.81	1.16	1.23	2.03	2.70	2.59	2.81	2.64	2.64	2.86	2.76	2.93	2.78
P_2O_5	1.03	1.03	0.91	0.66	0.82	0.81	0.00	0.34	0.34	0.28	0.41	0.41	0.40	0.38	0.30	0.29
Total	99.94	99.40	100.76	98.73	98.20	97.70	96.44	97.31	97.74	98.44	99.90	99.90	97.53	97.43	97.06	98.27
CO_2	b.d.l*	b.d.l*	-	-	-	-	-	-	b.d.l	-	b.d.l	-	-	b.d.l	b.d.l	
H_2O [1]	0.1*	0.3*	-	-	-	-	-	-	2.7	-	1.5	-	-	2.5	2.9	
H_2O [2]	0.06	0.60	-	1.27	1.80	2.30	3.56	2.69	2.26	1.56	0.10	0.10	2.47	2.57	2.94	1.73
Rb	62.1	54.1	40.1	64.8	34.6	17.1	84.1	n.a.	62.5	74.6	63.4	-	88.2	86.9	-	-
Sr	358	291	543	406	561	807	320	n.a.	291	280	325	-	333	307	-	-
Y	46.2	49.2	43.9	50.1	41.5	46.1	69.9	n.a.	56.0	65.7	48.8	-	57.5	57.9	-	-
Zr	265	260	271	418	237	231	571	n.a.	452	524	363	-	530	523	-	-
Nb	12.5	11.9	10.5	14.5	9.8	9.4	23.3	n.a.	20.0	20.0	18.8	-	25.0	24.5	-	-
Cs	2.48	2.22	3.48	2.93	1.31	b.d.l	2.03	n.a.	1.58	1.76	1.70	-	2.01	2.15	-	-
Ba	460	495	395	556	370	346	708	n.a.	816	632	773	-	739	719	-	-
La	28.5	29.5	28.0	36.6	26.0	25.4	43.4	n.a.	47.4	38.1	43.0	-	46.8	44.5	-	-
Ce	65.4	66.4	63.1	74.8	58.5	53.2	88.5	n.a.	90.2	89.6	91.8	-	106	104	-	-
Nd	41.9	42.5	42.7	45.9	37.3	36.1	50.4	n.a.	47.6	47.5	44.5	-	51.7	48.2	-	-
Sm	10.4	9.5	9.69	9.92	8.53	8.37	11.5	n.a.	9.48	10.6	9.2	-	10.6	10.3	-	-
Eu	2.79	2.19	3.10	2.78	2.55	2.68	2.83	n.a.	2.83	2.67	2.26	-	2.74	2.76	-	-
Yb	3.00	3.71	4.13	5.25	3.53	3.84	5.95	n.a.	5.50	5.30	0.96	-	5.60	5.99	-	-
Lu	0.68	0.64	0.54	0.53	0.62	0.67	1.00	n.a.	0.85	0.92	6.83	-	0.89	0.89	-	-

CO_2 and H_2O measured by FTIR are reported where analyzed.

1) H_2O as measured by FTIR. 2) H_2O by WBD method. * measured on other samples. b.d.l: beyond detection limits.

between 1,000 and 1,100°C. The lower P1 temperature from Fe-Ti oxide pairs, relative to the inferred temperature based on experimental data, may reflect pre-eruptive cooling and degassing of the melt as suggested by the numerous microlites in many of the pyroclasts (e.g., Taddeucci et al. 2004). The P2 temperature range, 970 to 976°C (average 972±26°C), was obtained from analyses of 17 magnetite-ilmenite pairs. Calculations also indicate a range of oxygen fugacity for the 1991 products. Oxygen fugacities range from −11.21 to −10.94 (±0.2) for P1, and from −10.29 (±0.16) to −10.42 (±0.18) for P2, just above the nickel–nickel oxide oxygen buffer.

Water content and pressure

Melt inclusion water contents were determined using FTIR and range from 1.0 to 3.0 wt% for P2 and 0.1 to 0.3 wt% for P1 (Table 5). Temperature and total H_2O were used to constrain magmatic pressures assuming water-saturated conditions (Moore et al. 1998). Inferred depths from these pressures range from <1 to 3.7 km for P2, and 0.1 to 0.3 km for P1. The pressure ranges are likely to be minimum values based on the evidence for degassing prior to eruption and the assumption of water-saturated conditions. The data thus suggest that the magmas produced during both phases of the 1991 activity may have been staged at relatively shallow levels in the crust prior to eruption.

Experimental analogues

Experimental studies of andesitic compositions provide important constraints on phase assemblages and melt compositions in crustal magma reservoirs (e.g., Luhr 1990; Barclay et al. 1998; Moore and Carmichael 1998;

Fig. 9 SiO$_2$ wt% variation in groundmass glass and melt inclusions from the P2 fall deposit units. The range of groundmass glass compositions becomes more mafic relative to the melt inclusions as the eruption progressed (60–65 wt% SiO$_2$). The melt inclusion range remains relatively constant (63–65 wt% SiO$_2$). Intervals on the scale bar in the photo are 10 cm apart. *Filled circles*: groundmass glasses; *open squares*: melt inclusions. In *parentheses* are total numbers of analyses for each unit. The melt inclusion data are from the same clast as the groundmass glass
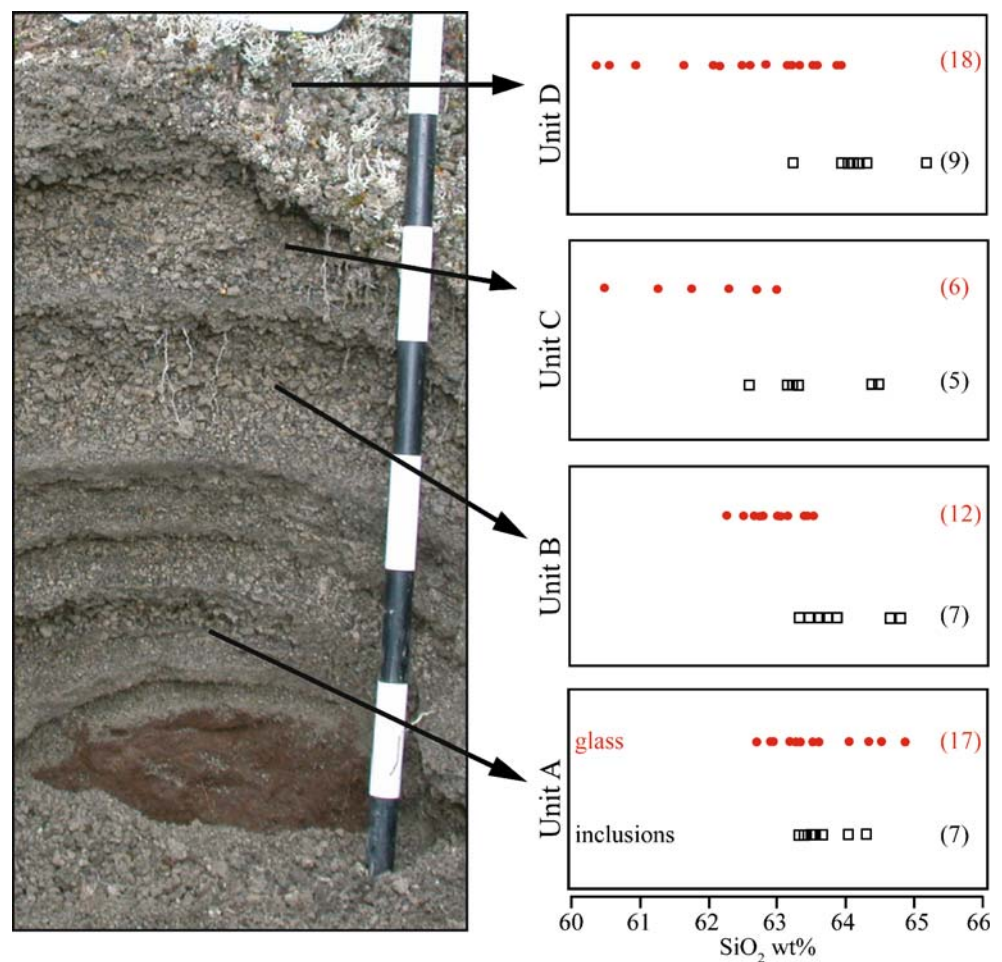
Martel et al. 1999). In particular, the experimental phase assemblages, degree of crystallization, and the water content in glasses can help to place tighter constraints on the location of the P2 chamber within the crust beneath Hudson volcano. Data on El Chichón (Luhr 1990), Mt. Pelée (Martel et al. 1999) and the Mexican Volcanic Belt (Moore and Carmichael 1998) fit the P2 compositions and inferred range of pressure/temperature conditions relatively well (supplementary Table S2), although none of the experimental compositions is a perfect match to the P2 trachyandesite.

Figure 12 shows the stability fields for the major mineral phases obtained from experimental work on andesite and trachyandesite compositions. In addition, the degree of crystallization from experimental work conducted on an andesite sample from Mascota, western Mexico, is shown as a series of points. All of the experiments were conducted under water-saturated conditions. The temperature of the Hudson P2 trachyandesite is well constrained at 972°C (±26) and the observed phase assemblage consists of plagioclase, clinopyroxene, Fe-Ti oxides, and minor olivine. At this temperature, the observed phase assemblage is
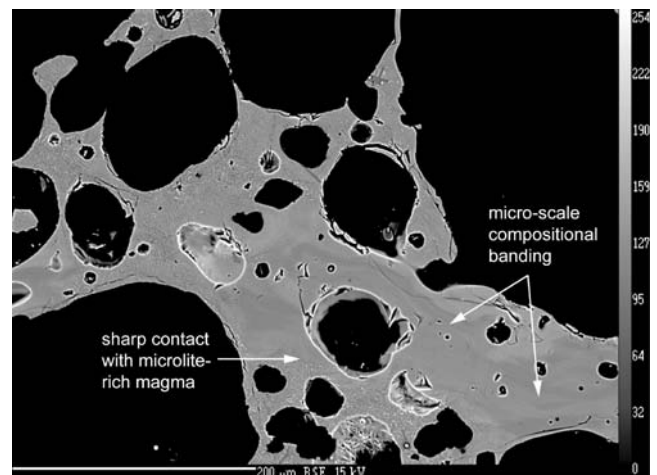
Fig. 10 Backscattered electron (BSE) image of a dark scoria sample from P2 unit D (sample HUD210) showing a sharp contact between microlite-rich and microlite-poor glass, presumed to result from physical mingling. Note the micro-scale compositional bands. Image has been adjusted using Adobe® Photoshop® CS3 to further highlight the bands
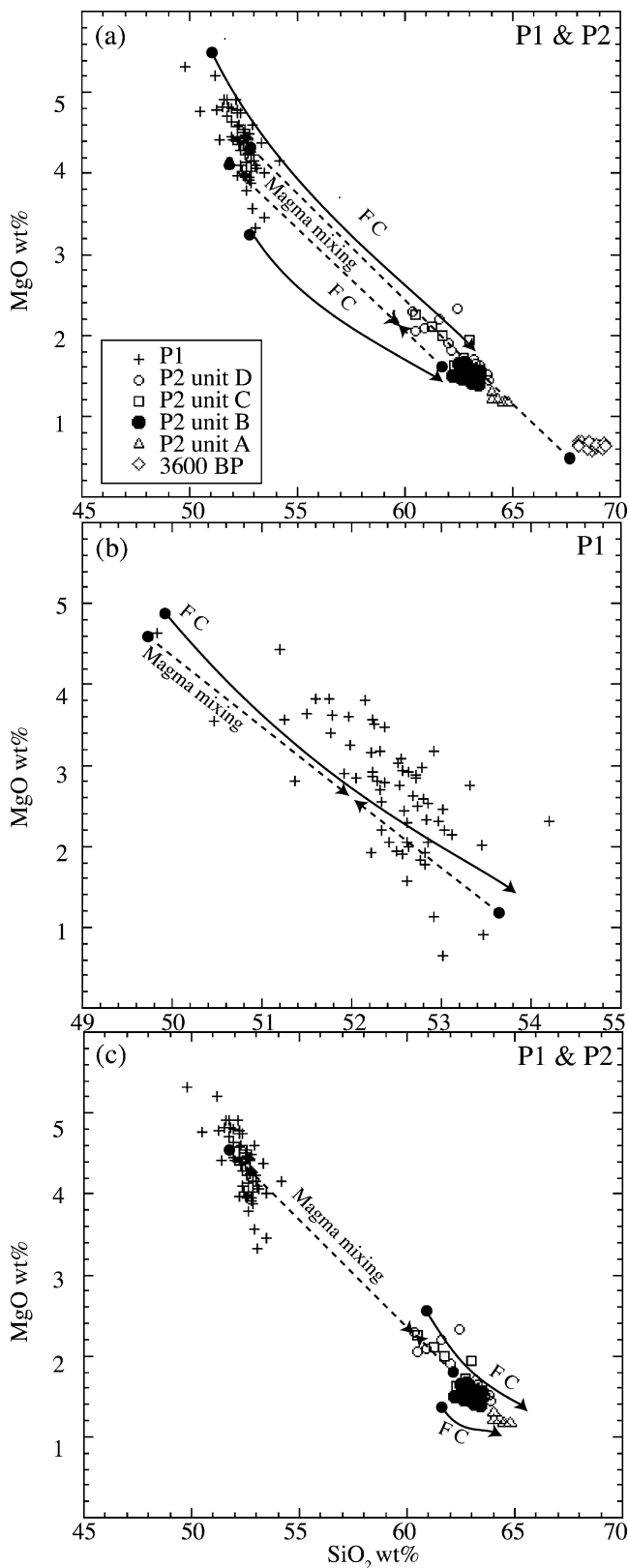
Fig. 11 Possible fractionation and/or mixing relationships between Hudson basaltic and trachyandesitic magmas, evaluated using geochemical models. The lines do not portray actual mixing or fractionation paths but serve to illustrate the end member compositions and the process evaluated. **a** Fractional crystallization (FC) of P1 basalt to yield P2 trachyandesite; mixing between P1 basalt and P2 trachyandesite (unit B) to yield the most mafic P2 trachyandesite (unit C); and mixing between P1 basalt and the 3,600 yrs BP trachyandesite to yield the P2 trachyandesite (unit B). **b** Compositional variations within the P1 groundmass glass modeled through both FC and magma mixing. **c** Magma mixing between P1 basalt and the dominant P2 trachyandesite (unit B) to yield the mafic trachyandesite of P2 (unit C); FC of the mafic trachyandesite to yield trachyandesite glasses of P2 (unit A); and FC of the dominant P2 trachyandesite (unit B) to yield the most evolved trachyandesite glasses (unit A)

closely matched by experiments at pressures below ~150 MPa (Fig. 12). The lack of amphibole in the Hudson products is an important constraint and suggests magma storage at relatively high temperatures. Amphibole was never found as a stable phase above 970°C at any pressure in the experiments. Inferred water contents in the glass inclusions from the P2 trachyandesite range from ~1 to 3 wt %. Based on the water solubility model of Moore et al. (1998), water saturation conditions would occur at pressures of 50 to 100 MPa, overlapping the range defined by the phase assemblage observations. At 975°C and 100 MPa pressure (–9.5 log fO_2) the glass produced by the Moore and Carmichael (1998) experiments contained 3.6 wt% H_2O, slightly higher than the upper limit for the water content of P2 melt inclusions (~3.0 wt%), implying storage at or below this pressure (water content increased with increasing pressure in the Moore and Carmichael (1998) experiments).

The extent of crystallization of the Hudson P2 samples was calculated using Igpet (Carr 2005) and ranges from 8.5 to 11.0 weight percent. These values are comparable to the experimental work of Moore and Carmichael (1998) (9–12 wt%) at pressures below 200 MPa (at 975°C) (Fig. 12). The experimental work suggests much higher degrees of crystallization if the magma was stored at lower pressures and a slightly higher temperature (e.g., 29 wt% at 1055 bars [~105 MPa] and 34 wt% at 441 bars [0.4 MPa], both at 1000°C). We conclude that the combination of observed phase assemblages, inferred water content, crystallinity, and geothermometry estimates strongly suggests pre-eruptive storage of the P2 trachyandesite at pressures between ~1.6 and ~3.3 kilometers depth, at 972±26°C and a log fO_2 of –10.33 (±0.2), under water-saturated conditions. The magma contained between 1.0 and 3.0 wt% H_2O, and 8.5–11.0 wt% crystals. Despite the relatively high water content, amphibole was not a stable phase due to the magma chamber temperature-pressure regime (Fig. 12).

Eruption model

A previously published model for the 1991 eruption of Hudson involved rising basaltic magma intersecting a shallow chamber prior to lateral diversion and subsequent eruption in the northwestern corner of the summit caldera (e.g., Naranjo et al. 1993). Naranjo et al. (1993) also suggested that basalt injection into a chamber containing more evolved trachyandesitic magma triggered the climactic phase (P2) of the 1991 eruption. Below we present a refined model for the eruption that is constrained by our new petrological and geochemical analysis.

We suggest that prior to the 1991 eruption, rising basaltic magma intersected the P2 storage region and mingled with the existing trachyandesitic magma (i.e., unit B composition). This influx may have led to overpressuring of the magma by pressure increase resulting from volatile exsolution, crystallization, and volatile oversaturation (e.g., Blake 1984), thus fracturing the chamber walls (Fig. 13a). The volumetrically minor basaltic magma eventually mixed with and hybridized the existing trachyandesite (e.g., Huppert et al. 1982). The extent of mixing between the two magmas diminished upwards from the lower parts of the chamber, based on the P2 melt inclusion/glass relationships (Fig. 9). Density differences between the basalt ($\sim$2,950 kg/m^3) and the trachyandesite ($\sim$2,600 kg/m^3) are likely to have resulted in restriction of the basalt to the lower part of the chamber, thus impeding its ability to rise directly to the surface through the existing P2 magma.

The fissure system associated with the P1 lava is oriented NNE–SSW, which coincides generally with the NE–SW striking local (i.e., meter-scale) faults around Hudson (Gutiérrez et al. 2005). Conversely, the P1 and P2 vents are located approximately 4 km apart on a NNW–SSE trend, paralleling the regional (i.e., kilometer-scale) tectonic lineaments (Gutiérrez et al. 2005). This stress regime may have been conducive to propagation of a basaltic dyke away from the trachyandesite reservoir. Another possibility is the reactivation of the 1971 eruption conduit system by the ascending P1 magma (e.g., Naranjo et al. 1993). We attribute the formation of the tachylite in the P1 products (Fig. 3b) to cooling or degassing, and suggest that the magma was stored close to the surface. The observed microlite morphologies (Fig. 3b) are similar to those produced in experimental studies of exsolution-induced crystallization (e.g., Hammer and Rutherford 2002). The eruption of lava during P1 may also be evidence for shallow pre-eruptive degassing of the magma. Both effusive and explosive phreatomagmatic eruptions of magma occurred at the NW vent (Fig. 13b). Although the phreatomagmatic phase of the P1 eruption may have produced some tachylite particles, such particles are not always a product of this style of eruption (e.g., Maria et al. 2000; Taddeucci et al. 2004).

The development of tachylite and the 4-day hiatus between eruption phases suggests that the volume of P1 basalt injected into the trachyandesite magma was not sufficient to immediately trigger the P2 eruption. The P1 eruption on April 8th and related seismicity may have allowed the already over-pressured P2 chamber to develop a pathway to the surface (directly above the reservoir) and begin an eruption from a vent $\sim$4 km south-southeast of the P1 vent (Fig. 13c). The general lack of tachylite in the P2 products suggests that the magma was withdrawn quickly from depth and did not stall at shallower levels. Additionally, the rising magma probably did not undergo significant cooling during ascent, as cooling would have led to amphibole crystallization, based on experimental phase relationships (Fig. 12). Alternatively, degassing and a reduction in volatiles would render amphibole unstable.

The near-simultaneous eruption of two distinct magma compositions from vents several kilometers apart, such as the 1991 Hudson eruption, provides compelling evidence for lateral magma injection. The concept of laterally propagating dykes intersecting crustal reservoirs and triggering an eruption while eruptions occurred simultaneously from another vent has been proposed for other volcanic centers including Askja in Iceland (Sparks et al. 1977) and Karymsky volcano, Kamchatka (Eichelberger and Izbekov 2000). Our new results from Hudson volcano provide additional evidence for the important role of basaltic magma injections into
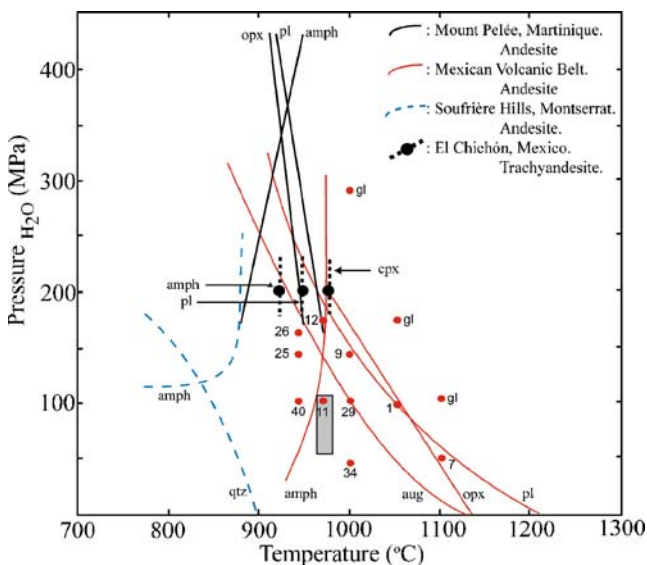

Fig. 12 Experimentally determined pressure-temperature phase diagram for andesitic compositions from El Chichón, Soufrière Hills, the Mexican Volcanic Belt and Mt. Pelée. *Filled red circles* and corresponding numbers are experimentally derived crystallinity values (weight percent) from Moore and Carmichael (1998); *gl*: glass. *Vertical gray bar* shows the range of P/T conditions inferred for the P2 trachyandesite based on geothermometry and volatile content estimations. Modified from Luhr (1990), Barclay et al. (1998), Moore and Carmichael (1998), and Martel et al. (1999)

Fig. 13 Model for the 1991 eruptions at Hudson volcano. a Rising basaltic magma intersects the P2 trachyandesitic storage region at between ~2–3 km depth. This injected basalt mixes with and hybridizes the magma near the base, and the extent of hybridization diminishes upwards. b Basaltic magma (P1) propagates in a dyke and stalls closer to the surface before erupting from a vent and fissure in the northwestern corner of the caldera. c Trachyandesite (P2) erupts explosively 4 days later from a vent approximately 4 km south-southeast of the P1 event
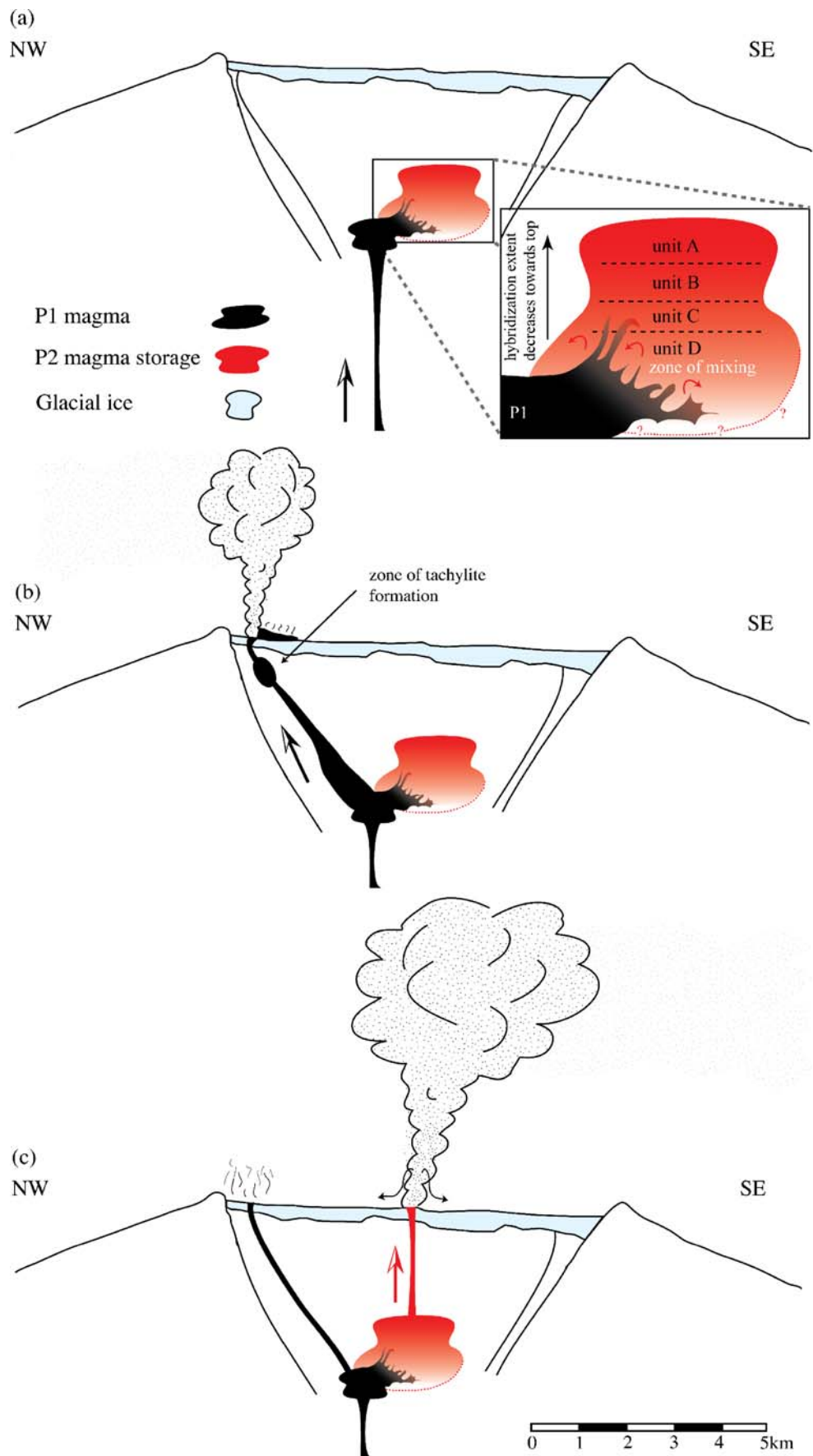
stable andesite chambers beneath arc volcanoes and the complex pathways that develop. Evidence of the nature of the interactions is preserved in the variations in magma composition, phase assemblages, and melt inclusion relationships that occur within separate eruption sequences.

Conclusions

The 1991 eruptions of Hudson volcano in Chile involved the near simultaneous discharge of compositionally distinct basalt (P1) and trachyandesite (P2) magma at different vents. A combination of petrographic features and geochemical modeling suggests that the P1 basaltic and P2 trachyandesitic magmas were related through a combination of magma mixing and fractional crystallization. The main volume of trachyandesite is likely to have been produced by fractionation of olivine, clinopyroxene, plagioclase and Fe-Ti oxides from basaltic magma with compositional characteristics similar to P1 basalts or other basalts produced during the eruptive history of Hudson. Compositional variations of the melt phase identified in the P2 fallout sequence can be produced through fractionation of plagioclase, pyroxene and Fe-Ti oxides, and partial modification through magma mixing with basalt prior to eruption. Pre-eruptive storage of the P2 trachyandesite occurred at pressures between ~50–100 MPa at approximately 972°C (±26) and log fO_2 –10.33 (±0.2), under water-saturated conditions based on estimates of volatile content in melt inclusions, mineral geothermometry, and comparisons to experimental work.

We propose that rising basaltic magma, erupted during P1, intersected the trachyandesite storage region between 2 and 3 km depth and partially mixed with, and hybridized the existing magma. Mixing appears to have been restricted to the lower parts of the chamber (last erupted material) and was likely controlled by the greater density of the basalt relative to the trachyandesite, and the amount of time between the initial interaction of the magmas and their subsequent discharge during the evolution of the eruption. Following the interaction of basalt and trachyandesite in the magma storage region, basalt continued to rise towards the surface in a lateral fashion along a NNW–SSE trend, possibly exploiting regional zones of weakness. Abundant tachylite in the P1 products suggests that magma was stored at shallow depths (<0.5 km) prior to eruption on August 8th at a vent in the northwest corner of Hudson caldera.

The increase in volume and potential volatile exsolution associated with mixing between basalt and trachyandesite may have led to overpressure within the storage region and triggering of the P2 eruption, which occurred on August 12th from a vent 4 km south-southeast of the P1 vent. Ascent of magma during this phase of the eruption must have been relatively rapid, as the products of the P2 event do not include tachylite. The trachyandesitic glasses exhibit a systematic increase in compositional heterogeneity and became progressively more mafic as the P2 eruption continued, reflecting variations in the extent of hybridization induced by mixing with P1 basalt.

References

Andersen DJ, Lindsley DH (1988) Internally consistent solution models for Fe-Mg-Mn-Ti oxides: Fe-Ti oxides. Am Mineral 73(7–8):714–726

Andersen DJ, Lindsley DH, Davidson PM (1993) QUILF: a Pascal program to assess equilibria among Fe-Mg-Mn-Ti oxides, pyroxenes, olivine, and quartz. Comp Geosci 19:1333–1350

Araujo MA (1993) Participacion del INPRES en el monitoreo sismologico de volcanes. I Jorn Nac Vilcan Med Amb Def Civ Actas 157–160

Bacon CR, Hirschmann MM (1988) Mg/Mn partitioning as a test for equilibrium between coexisting Fe-Ti oxides. Am Mineral 73:57–61

Barclay J, Rutherford MJ, Carroll MR, Murphy MD, Devine JD, Gardner JE, Sparks RSJ (1998) Experimental phase equilibria constraints on pre-eruptive storage conditions of the Soufrière Hills magma. Geophys Res Lett 25(18):3437–3440

Bitschene PR, Fernández MI (1995) Volcanology and petrology of fallout ashes from the August 1991 eruption of the Hudson Volcano (Patagonian Andes). In: Bitschene PR, Mendia J (eds) The August 1991 eruption of the Hudson Volcano (Patagonian Andes); a thousand days after. Cuvillier, Göttingen, pp 27–54

Bitschene PR, Fernández MI, Arias N, Arizmendi A, Griznik M, Nillni A (1993) Volcanology and environmental impact of the August 1991 eruption of the Hudson volcano (Patagonian Andes, Chile). Zbl Geol Palaont Teil I H 1/2:165–177

Blake S (1984) Volatile oversaturation during the evolution of silicic magma chambers as an eruption trigger. J Geophys Res 89(B10):8237–8244

Carr M (2005) Igpet for Windows. CD-ROM

Davidson J, Hassanzadeh J, Berzins R, Stockli DF, Bashukooh B, Turrin B, Pandamouz A (2004) The Geology of Damavand Volcano, Alborz Mountains, Northern Iran. Bull Geol Soc Am 116:16–29

Davidson JP, Morgan DJ, Charlier BLA, Harlou R, Hora JM (2007) Microsampling and isotopic analysis of igneous rocks: implications for the study of magmatic systems. Ann Rev Earth Planet Sci 35(1):273–311

Devine JD, Gardner JE, Brack HP, Layne GD, Rutherford MJ (1995) Comparison of microanalytical methods for estimating H_2O contents of silicic volcanic glasses. Am Mineral 80:319–328

Eichelberger JC (1975) Origin of andesite and dacite: evidence of mixing at Glass Mountain in California and at other Circum-Pacific volcanoes. Geol Soc Am Bull 86:1381–1391

Eichelberger JC, Izbekov PE (2000) Eruption of andesite triggered by dyke injection: contrasting cases at Karymsky Volcano, Kamchatka and Mt Katmai, Alaska. Phil Trans R Soc Lond 358:1465–1485

Forsythe RD, Nelson EP (1985) Geological manifestations of ridge collision: evidence from the Golfo de Penas-Taitao basin, southern Chile. Tectonics 4:477–495

Gutiérrez F, Gioncada A, Gonzalez-Ferran O, Lahsen A, Mazzuoli R (2005) The Hudson volcano and surrounding monogenetic centres (Chilean Patagonia): an example of volcanism associated with ridge-trench collision environment. J Volcanol Geotherm Res 145:207–233

Hammer JE, Rutherford MJ (2002) An experimental study of the kinematics of decompression-induced crystallization in silicic melt. J Geophys Res 107(B1):1–24

Huppert HE, Sparks RSJ, Turner JS (1982) Effects of volatiles on mixing in calc-alkaline magma systems. Nature 297:554–557

Irvine TN, Baragaar WRA (1971) A guide to the chemical classification of the common volcanic rocks. Can J Earth Sci 8 (5):523–548 doi:10.1139/e71–055

Izbekov PE, Eichelberger JC, Patino LC, Vogel TA, Ivanov BV (2002) Calcic cores of plagioclase phenocrysts in andesite from Karymsky volcano: evidence for rapid introduction by basaltic replenishment. Geology 30(9):799–802

Kelley KA, Plank T, Ludden J, Staudigel H (2003) Composition of altered oceanic crust at ODP Sites 801 and 1149. Geochemistry, Geophysics, Geosystems 4(6):8910 doi:10.1029/2002GC000435

Lautze NC, Houghton BF (2005) Physical mingling of magma and complex eruption dynamics in the shallow conduit at Stromboli volcano, Italy. Geology 33(5):425–428 doi:10.1130/G21325.1

Luhr JF (1990) Experimental phase relations of water- and sulfur-saturated arc magmas and the 1982 eruptions of El Chichón volcano. J Petrol 31(5):1071–1114

Mandeville CW, Webster JD, Rutherford MJ, Taylor BE, Timbal A, Faure K (2002) Determination of molar absorptivities for infrared absorption bands of H$_2$O in andesitic glasses. Am Mineral 87:813–821

Maria A, Carey S, Sigurdsson H, Kincaid C, Helgadottir G (2000) Source and dispersal of jökulhaup sediments discharged to the sea following the 1996 Vatnajökull eruption. Geol Soc Am Bull 112(10):1507–1521

Martel C, Pichavant M, Holtz F, Scaillet B, Bourdier J-L, Traineau H (1999) Effects of fO2 and H$_2$O on andesite phase relations between 2 and 4 kbar. J Geophys Res 104(B12):29,453–429,470 doi:0.1029/1999JB900191

Martel C, Radadi Ali A, Poussineau S, Gourgard A, Pichavant M (2006) Basalt-inherited microlites in silicic magmas: evidence from Mount Pelée (Martinique, French West Indies). Geology 34 (11):905–908 doi:10.1130/G22672A.1

Moore G, Carmichael ISE (1998) The hydrous phase equilibria (to 3 kbar) of an andesite and basaltic andesite from western Mexico: constraints on water content and conditions of phenocryst growth. Contrib Mineral Petrol 130:304–319 doi:10.1007/s004100050367

Moore G, Vennemann T, Carmichael ISE (1998) An empirical model for the solubility of H$_2$O in magmas to 3 kilobars. Am Mineral 83:36–42

Murphy MD, Sparks RSJ, Barclay J, Carroll MR, Lejeune A-M, Brewer TS, Macdonald R, Black S, Young SR (1998) The role of magma mixing in triggering the current eruption at the Soufrière Hills volcano, Montserrat, West Indies. Geophys Res Lett 25 (18):3433–3436

Naranjo JA, Moreno H, Banks N (1993) La erupción del Volcán Hudson en 1991 (46°S), Región XI, Aisén. Chile Boletin 44:1–50

Naranjo JA, Stern CR (1998) Holocene explosive activity of Hudson Volcano, southern Andes. Bull Volcanol 59:291–306 doi:10.1007/s004450050193

Orihashi Y, Naranjo JA, Motoki A, Sumino H, Hirata D, Anma R, Nagao K (2004) Quaternary volcanic activity of Hudson and Lautaro volcanoes, Chilean Patagonia: new constraints from K-Ar ages. Rev Geol Chile 31(2):207–224

Pallister JS, Hoblitt RP, Reyes AG (1992) A basalt trigger for the 1991 eruptions of Pinatubo volcano? Nature 356:426–428 doi:10.1038/356426a0

Scasso RA, Carey S (2005) Morphology and formation of glassy volcanic ash from the August 12–15, 1991 eruption of Hudson Volcano, Chile. Lat Am J Sedimentol Bas Anal 12(1):3–21

Scasso RA, Corbella H, Tiberi P (1994) Sedimentological analysis of the tephra from the 12–15 August 1991 eruption of Hudson volcano. Bull Volcanol 56:121–132 doi:10.1007/BF00304107

Sparks RSJ, Sigurdsson H, Wilson L (1977) Magma mixing: a mechanism for triggering acid explosive eruptions. Nature 267:315–318

Stern CR (1991) Mid-Holocene tephra on Tierra del Fuego (54°S) derived from the Hudson Volcano (46°S): evidence for a large explosive eruption. Rev Geol Chile 18(2):139–146

Stern CR (2004) Active Andean volcanism: its geologic and tectonic setting. Rev Geol Chile 31(2):161–206

Stern CR, Futa K, Muehlenbachs K (1984) Isotope and trace element data for orogenic andesites from the Austral Andes. In: Harmon RS & Barreiro BA (eds) Andean magmatism: chemical and isotopic constraints. Shiva Geology Series, pp 31–46

Taddeucci J, Pompolio M, Scarlato P (2004) Conduit processes during the July–August 2001 explosive activity of Mt. Etna (Italy): inferences from glass chemistry and crystal size distribution of ash particles. J Volcanol Geotherm Res 137:33–54 doi:10.1016/j.jvolgeores.2004.05.011

Tepley FJ III, Davidson JP, Tilling RI, Arth JG (2000) Magma mixing, recharge and Eruption Histories Recorded in Plagioclase Phenocrysts from El Chichón Volcano, Mexico. J Petrol 41(9):1397–1411

Venezky DY, Rutherford MJ (1999) Petrology and Fe-Ti oxide reequilibration of the 1991 Mount Unzen mixed magma. J Volcanol Geotherm Res 89(1–4):213–230 doi:10.1016/S0377–0273(98)00133–4

Wilson M (1989) Igneous Petrogenesis. Kluwer Academic Publishers, Boston, MA